848

Pulsed Interleaved Excitation Fluctuation Imaging

Jelle Hendrix,[†*] Waldemar Schrimpf,[†] Matthias Höller,[†] and Don C. Lamb[†‡*]
[†]Physical Chemistry, Department of Chemistry, Munich Center for Integrated Protein Science and Center for Nanoscience, Ludwig-Maximilians-Universität München, Munich, Germany; and [‡]Department of Physics, University of Illinois at Urbana-Champaign, Urbana, Illinois

ABSTRACT   Fluorescence fluctuation imaging is a powerful means to investigate dynamics, interactions, and stoichiometry of proteins inside living cells. Pulsed interleaved excitation (PIE) is the method of nanosecond alternating excitation with time-resolved detection and allows accurate, independent, and quasi-simultaneous determination of fluorescence intensities and life-times of different fluorophores. In this work, we combine pulsed interleaved excitation with fluctuation imaging methods (PIE-FI) such as raster image correlation spectroscopy (RICS) or number and brightness analysis (N&B). More specifically, we show that quantitative measurements of diffusion and molecular brightness of Venus fluorescent protein (FP) can be performed in solution with PIE-RICS and compare PIE-RICS with single-point PIE-FCS measurements. We discuss the advantages of cross-talk free dual-color PIE-RICS and illustrate its proficiency by quantitatively comparing two commonly used FP pairs for dual-color micro-scopy, eGFP/mCherry and mVenus/mCherry. For N&B analysis, we implement dead-time correction to the PIE-FI data analysis to allow accurate molecular brightness determination with PIE-NB. We then use PIE-NB to investigate the effect of eGFP tan-dem oligomerization on the intracellular maturation efficiency of the fluorophore. Finally, we explore the possibilities of using the available fluorescence lifetime information in PIE-FI experiments. We perform lifetime-based weighting of confocal images, allowing us to quantitatively determine molecular concentrations from 100 nM down to <30 pM with PIE-raster lifetime image correlation spectroscopy (RLICS). We use the fluorescence lifetime information to perform a robust dual-color lifetime-based FRET analysis of tandem fluorescent protein dimers. Lastly, we investigate the use of dual-color RLICS to resolve codiffusing FRET species from non-FRET species in cells. The enhanced capabilities and quantitative results provided by PIE-FI make it a powerful method that is broadly applicable to a large number of interesting biophysical studies.

INTRODUCTION

As of this writing, there is a large push in the biophysical sciences to extract more information from individual experiments and perform more-quantitative analyses. One of the tools that is routinely used to investigate biomolecular mobility, concentration, and interactions in vitro and in live cells is fluorescence fluctuation spectroscopy (FFS). FFS started with fluorescence correlation spectroscopy (FCS) in the early 1970s, which quantifies fluctuations in fluorescence intensity with time (1–3). The introduction of fast confocal laser scanning microscopy (CLSM) in the second half of the 1980s (4) made it possible to deter-mine molecular properties in a spatio-temporally resolved manner, but it took several years before the FFS methodology was combined with CLSM to perform fluorescence fluctuation imaging (FFI). The earliest report of FFI was image correlation spectroscopy (ICS) in which the size and concentration of immobile molecular aggregates were determined by spatial correlation analysis (5). Many devel-opments of the ICS method have appeared in literature, including, quantitative analysis of temporal and spatio-temporal fluorescence intensity variations in CLSM images and/or image series (6,7).

Dual-color FFI techniques allow detailed investigations of the interactions of differentially labeled molecules from images at the ensemble (7–10) and single-molecule level (11). However, multicolor imaging systems typically suffer from crosstalk (or spectral bleed-through) of photons from the more blue-shifted fluorophore into the detection channel of the red-shifted fluorophore. Crosstalk reduces the sensi-tivity and dynamic range of multicolor FFI and complicates data analysis. In the mid-2000s, methodologies in which excitation lasers were alternated on the microsecond (alter-nating laser excitation, ALEX) and nanosecond timescales (pulsed interleaved excitation, PIE) were introduced to allow quasi-simultaneous and independent multicolor imaging (12,13). Combining ALEX or PIE with established fluorescence techniques has been proven to increase their sensitivity and robustness considerably. For example, with PIE it is possible to perform quantitative point fluorescence cross-correlation spectroscopy measurements, even when the sample undergoes Förster resonance energy transfer (FRET) (13). PIE also allows us to perform highly accurate single-pair FRET experiments when combined with multi-parameter fluorescence detection (14).

In this work, we describe the advantages and challenges of combining PIE with fluctuation imaging (PIE-FI). In particular, we combined PIE with raster ICS (RICS) and the number and brightness (N&B) analysis method (15,16). RICS exploits the spatio-temporal information en-coded in a single CLSM image to extract the diffusion coef-ficient and concentration of fast diffusing molecules (15). N&B makes it possible to determine the concentration and stoichiometry of fast diffusing molecular complexes (16).

CrossMark

We use PIE-RICS to investigate diffusion of the Venus fluorescent protein (FP) (17) under different conditions and compare the performance of two interesting FP pairs with dual-color PIE-FI on tandem heterodimers of eGFP-mCherry and mVenus-mCherry in cells. We also combine PIE with N&B to measure a fluorophore-specific absolute brightness and apply PIE-NB to studying eGFP oligomer maturation inside cells. Finally, we exploit the available fluorescence lifetime information for dual-color fluorophore-specific lifetime imaging and for a lifetime-weighted RICS analysis. We apply the latter approach to 1), measure concentrations accurately in vitro in the pM range with single-color PIE-RICS; and 2), to resolve dual-color codiffusing FRET species from non-FRET species based on their fluorescence lifetime with dual-color PIE-RICS in cells.

MATERIALS AND METHODS

Details of the reagents used, sample preparation, and cell culture can be found in the Supporting Material.

Microscopy

All experiments were performed on a home-built, dual-color PIE dual-color detection microscope (see Fig. S1 in the Supporting Material). Laser powers in this work were measured in the excitation path; the total laser power at the sample was ~40% of this value. The point-spread function (PSF) was always positioned close to the coverslip (<10 μm), to limit refractive-index related problems (18). Unless stated otherwise, the (12.5-μm)^2-sized images were recorded at (300-pixel)^2 resolution and 1-s time frame (pixel size $\delta r = 41.7$ nm, pixel dwell time $\tau_p = 11.11$ μs, line time $\tau_l = 3.333$ ms). Per experiment, 5–400 frames were recorded depending on the concentration and brightness of the molecules under investigation. Data analysis was performed with software written in the software MATLAB (The MathWorks, Ismaning, Germany), which is available upon request and can be used to analyze fluctuation images obtained with most (also non-PIE) CLSMs. More details of the setup are given in the Supporting Material.

RESULTS AND DISCUSSION

Robust measurement of fluorescent protein diffusion with PIE-RICS

RICS with PIE-FI

To test for potential effects of pulsed excitation on RICS data, we performed PIE-FI experiments on Venus fluorescent protein (FP) diluted in aqueous buffer. We recorded photons with 475-nm pulsed excitation and dual-color detection, while performing rapid laser scanning of 100 image frames (see Materials and Methods for imaging settings). Because the arrival time of all photons with respect to the exciting laser pulse is available with PIE, the data can be represented directly in a microscopic arrival time histogram per detector, which we will refer to as a microtime histogram (Fig. 1 A). The majority of photons were detected in the green detection channel (Fig. 1 A, top panel) and ~13% of

the total emission of Venus FP was detected as crosstalk in the red detection channel (Fig. 1 A, lower panel). This value is close to what is expected based on the known absorption coefficients and quantum yield of Venus FP and filters and transmission coefficients of the setup (see Table S1 and Fig. S2 in the Supporting Material). Next, we used time gating (19) to perform further analysis only with photons detected in a specific PIE channel (Fig. 1 A, gray hatched areas). Photons in the $F_{\mathrm{GG}}(t)$ PIE channel include green emission photons after 475-nm excitation of the green fluorophore and photons in the $F_{\mathrm{GR}}(t)$ PIE channel include red emission photons after 475-nm excitation. With the scantiming information available as well as the arrival times of all recorded photons with respect to the start of the experiment (i.e., macrotimes), we constructed a macrotime image series, $I_{\mathrm{GG}}(x,y,f)$, where GG denotes the $F_{\mathrm{GG}}(t)$ PIE channel; x- and y- are the fast and slow scanning axis of the laser, respectively; and f is the number of the image frame. The average macrotime image is displayed in Fig. 1 B. The homogeneous intensity over the field of view suggests that the PSF is uniform throughout the image. We verified this uniformity quantitatively with point FCS measurements (see Fig. S3). We subsequently used $I_{\mathrm{GG}}(x,y,f)$ to calculate a series of spatial autocorrelation functions (ACFs),

$$G(\xi,\psi,f) = \frac{\langle I_1(x,y,f)I_2(x+\xi,y+\psi,f)\rangle_{XY}}{\langle I_1(x,y,f)\rangle_{XY}\langle I_2(x,y,f)\rangle_{XY}}, \quad (1)$$

where ξ and ψ are the spatial lag (in pixels), and

$$\langle I \rangle_{XY} = (XY)^{-1}\sum_{y=1}^{Y}\sum_{x=1}^{X} I$$

is the spatial average intensity with X and Y being the respective dimensions of the image; $I_1 = I_2$ for an autocorrelation analysis; and $I_1 \neq I_2$ when two different images are used for a cross-correlation analysis. A fast Fourier transform algorithm (5) was used for calculating $G(\xi,\psi,f)$ and the resulting two-dimensional ACF series was averaged over all image frames F. A typical average two-dimensional ACF, $\langle G(\xi,\psi)\rangle_F$, of Venus FP in solution is shown in Fig. 1 C (top view) and in Fig. 1 D (side view). The central region (30 × 30 to 50 × 50 pixels) in $\langle G(\xi,\psi)\rangle_F$ was fitted with a RICS model for free diffusion in a three-dimensional Gaussian point-spread function (PSF) (8),

$$G_{\mathrm{RICS},D}(\xi,\psi) = \frac{\gamma}{N}\left(1 + \frac{4D(\tau_p\xi + \tau_l\psi)}{\omega_r^2}\right)^{-1}$$
$$\times \left(1 + \frac{4D(\tau_p\xi + \tau_l\psi)}{\omega_z^2}\right)^{-1/2}\exp\left(-\frac{\delta r^2(\xi^2 + \psi^2)}{\omega_r^2 + 4D(\tau_p\xi + \tau_l\psi)}\right),$$
$$(2)$$

where $\gamma = 2^{-3/2}$ is the geometrical factor for a three-dimensional Gaussian PSF (20,21); N is the average number of molecules in the PSF; D is the diffusion coefficient; τ_p is
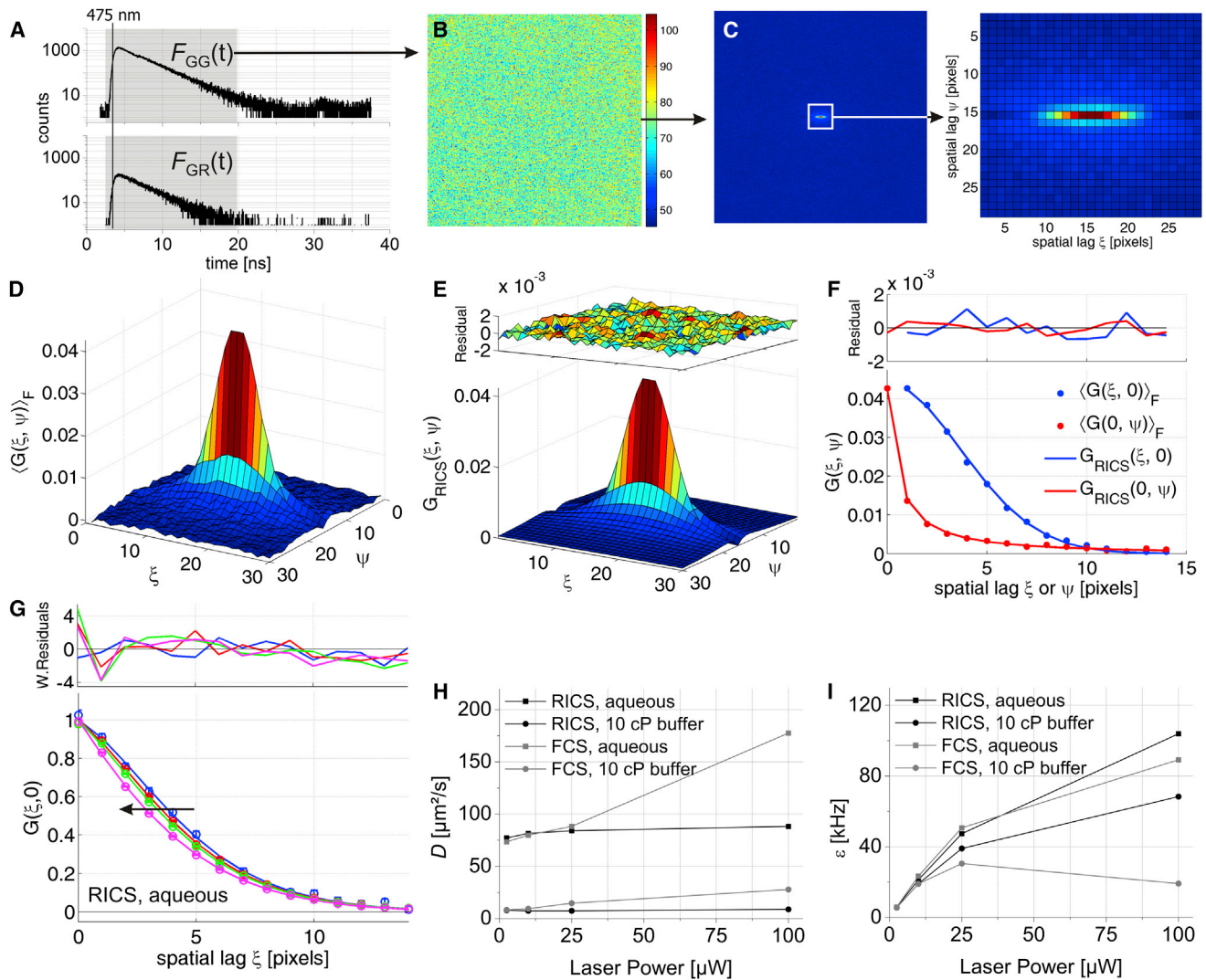
FIGURE 1   PIE-RICS experiments on Venus FP. (*A*) Logarithmic microtime histograms of all photons detected in the green (*top*) and red (*bottom*) detection channel during five images. (*Gray hatching*) The different PIE channels. (*B*) The average macrotime image ($F = 100$) with photons detected in the $F_{GG}(t)$ PIE channel from 100-nM Venus FP freely diffusing in buffer and measured at 5 μW excitation power. (*C*) Typical average spatial ACF of the data in panel *B*. (*D*) Three-dimensional representation of the data plotted in panel *C*. (*E*) Three-dimensional fit and residual plot for the 100-nM Venus ACF plotted in panels *C* and *D*. (*F*) The *x*- and *y*-cross sections of the RICS correlation function, fit, and residuals for the data plotted in panels *C* and *D*. (*G*) Experimental $G(\xi,0)$ from RICS (*symbols*) at 2.5 (*blue*), 10 (*red*), 25 (*green*), and 100 μW (*pink*) excitation power in an aqueous buffer. (*Solid line*) Fit to Eq. 3. (*Plot* on the *upper panel*) Weighted residuals. (*Black arrow*) Trend with increasing laser power. To allow a direct comparison of their shape, the correlation functions were normalized to the amplitude of the fit function by multiplying the data and fit with $N(1-F_b)\gamma^{-1}$. (*H* and *I*) The apparent diffusion coefficient (*H*) and brightness (*I*) of Venus FP are plotted as a function of laser power. The results from single-point FCS experiments are shown for comparison.

the pixel dwell time; τ_l is the line time; $\omega_r \approx 0.2$ μm and $\omega_z \approx 1$ μm are the radial and axial dimensions of the PSF, respectively; and δr is the pixel size. The size of the PSF was determined by point FCS measurements on reference dyes. Because fast scanning increases the effective lateral PSF size, where possible, ω_r was used as a fitting parameter in addition to N and D. To show both the data as well as the fit in the same graph, it is useful to show only the $G(\xi,0)$ or $G(0,\psi)$ correlation curves (Fig. 1 *F*). Because photon counting detectors do not exhibit afterglowing (in contrast to analog photomultiplier tubes) (22), only

$G(0,0)$ has to be omitted from the fitting for ACFs calculated from a single APD.

Diffusion coefficient measurements

Because fast photophysics (blinking, photobleaching) of yellow FPs is known to render quantitative estimations of D difficult when measured with FCS (23), we verified the performance of PIE-RICS for measuring D of Venus FP by measuring the laser power dependence of $\langle G(\xi,\psi) \rangle_F$ in an aqueous buffer. A shift of the spatial ACF to a faster timescale was observed when increasing the laser power

(Fig. 1 G). We fitted the resulting data with a RICS model including a blinking term,

$$G_{\text{RICS}}(\xi, \psi) = \left[1 + \frac{F_b}{1 - F_b} \exp\left(\frac{\tau_p \xi + \tau_l \psi}{\tau_b} \right) \right] G_{\text{RICS},D}(\xi, \psi), \quad (3)$$

where F_b and τ_b are the fractional amplitude and relaxation time of the fast process, respectively, and $G_{\text{RICS}}(\xi, \psi)$ is the normal RICS model from Eq. 2. Furthermore, we performed complementary (PIE-)FCS and PIE-RICS experiments both in an aqueous buffer and in a more viscous sucrose/buffer mixture (10-cP buffer) that mimics free cellular diffusion of Venus FP and determined the apparent D (Fig. 1 H and see Fig. S4). Clearly, D depended much less on the laser power when measured with PIE-RICS. The average D in aqueous buffer was determined to be 82.8 ± 4.6 μm^2/s and in the 10-cP buffer 7.8 ± 0.7 μm^2/s.

Brightness determination

For the same experiments on Venus FP, we determined the apparent peak molecular brightness ε at the center of the PSF (20,21,24) by dividing the average count rate by N:

$$\varepsilon[\text{kHz}] = \frac{\langle I \rangle[\text{kHz}]}{N}. \quad (4)$$

The maximum apparent molecular brightness that could be achieved with PIE-RICS as a function of laser power was much higher for PIE-RICS than with FCS (Fig. 1 I and see Fig. S4). When PIE-RICS was performed with all photons detected after blue excitation by using the summed $F_{\text{GG+GR}}(t) = F_{\text{GG}}(t) + F_{\text{GR}}(t)$ time gate, the obtained D and N stayed the same (data not shown) but the brightness was larger by ~10% (10.3 kHz/mol at 5 μW excitation power) as compared to the complementary RICS analysis with photons from the $F_{\text{GG}}(t)$ time gate (9.2 kHz/mol).

Hence, it is possible to perform quantitative RICS measurements with PIE. Interestingly, PIE-RICS measurements on Venus FP were more robust than point PIE-FCS experiments. The fast laser scanning used with PIE-RICS limits the total illumination time per FP, allowing it to cope better with blinking and/or bleaching and, as a result, yields a higher maximal apparent brightness and correct D at higher laser intensities (Fig. 1, H and I). Therefore, it would be the method of choice for accurately measuring FPs with considerable dark state formation, such as mRFP1 or mCherry (25). Additionally, when measuring in cells, RICS provides the advantage of acquiring a spatially averaged D. Conversely, point FCS would provide a much more precise choice of the measurement location and would be preferable when the sample exhibits localized fluctuating image heterogeneities that cannot be removed from the image series by preprocessing the data before the RICS analysis. Other scanning-based techniques such as line- or circle-FCS could also be used to circumvent blinking or bleaching problems

(26,27). Finally, because ω_r is an independent fitting parameter in RICS, it allows an accurate quantification of D, as has been shown before for dual-foci scanning FCS (27). Alternatively, two-focus FCS also provides accurate measurements of D with high spatial resolution and benefits from the full time resolution of FCS (28). However, two-focus FCS is still sensitive to artifacts due to fast fluorophore photophysics and care should be taken when performing any fluorescence fluctuation method with fluorescent proteins.

Imaging protein-protein interactions in living cells with dual-color PIE-RICS

Dual-color RICS with PIE-FI

The real advantage of PIE-FI comes when multicolor and/or lifetime imaging experiments are performed. To demonstrate the possibilities of PIE when multiple excitation wavelengths are used, we performed PIE-FI on HeLa cells expressing eGFP and mCherry FP and analyzed the data with the cross-correlation RICS method (ccRICS) (8). The emission of eGFP after 475-nm excitation is detected in the $F_{\text{GG}}(t)$ and $F_{\text{GR}}(t)$ PIE channels, while the red emission photons of mCherry excited with interleaved 561-nm excitation are detected in the $F_{\text{RR}}(t)$ PIE channel (Fig. 2 A). Put simply, direct mCherry emission and crosstalk of the eGFP are temporally separated in the red detection channel. Next, we determined the eGFP and mCherry-specific macrotime images from the $F_{\text{GG}}(t)$ and $F_{\text{RR}}(t)$ PIE channels, respectively, to show the specific cellular distribution of both fluorophores in the absence of crosstalk (Fig. 2 B). Then, a portion of the cell was selected for the RICS analysis (Fig. 2 B, white squares). Before image correlation with Eq. 1, macrotime images were spatially homogenized with a 10-frame moving average correction (Eq. S3 in the Supporting Material) (29). This homogenization is necessary to ensure that spatial correlations within images are only caused by fast diffusing molecules. The result of spatial correlation analysis with macrotime images calculated from different PIE channels is displayed in Fig. 2 C.

The spatial ACF of the red fluorophore in the presence of crosstalk

The amplitude of the red non-PIE spatial ACF $G_{\text{GR+RR}}$ calculated from images containing all red detected photons (Fig. 2 C, dark red curve) is given by

$$G_{\text{GR+RR}}(0,0) = \left(\frac{f_{\text{G}_\text{T},\text{R}_\text{T}}\beta^2 + 2\beta f_{\text{GR},\text{R}_\text{T}} + 1}{\left(\beta f_{\text{G}_\text{T},\text{R}_\text{T}} + 1 \right)^2} \right) \frac{1}{N_{\text{R}_\text{T}}}, \quad (5)$$

where $f_{\text{G}_\text{T},\text{R}_\text{T}}$ is the ratio of total green versus total red molecules in the PSF; $f_{\text{GR},\text{R}_\text{T}}$ is the ratio of double-labeled versus total red molecules; β is the crosstalk parameter describing the relative brightness of the green versus red fluorophore in macrotime images calculated with photons from the
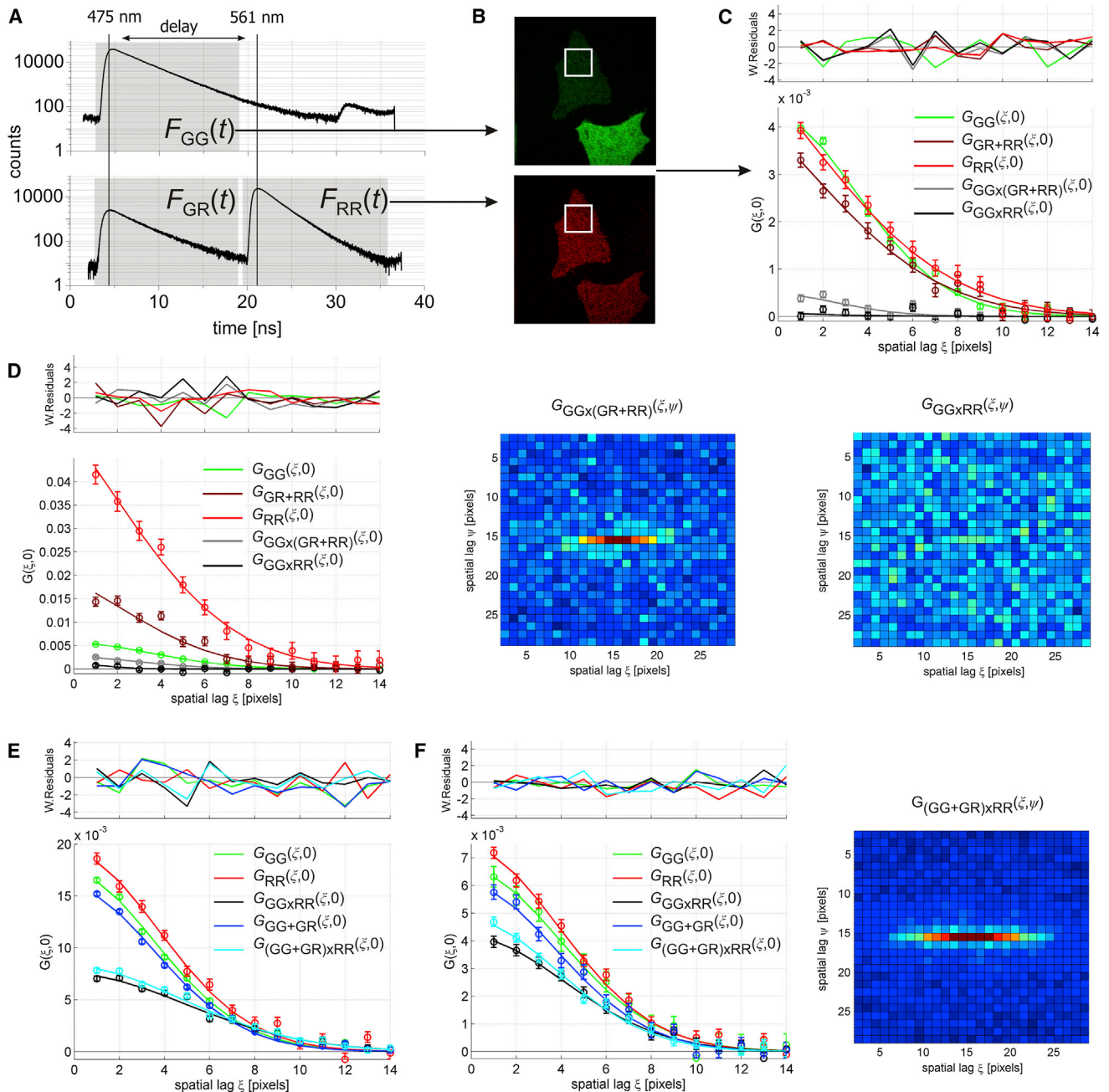
FIGURE 2   Dual-color PIE-RICS in the cytosol of living HeLa cells. (A) Logarithmic microtime histograms recorded in cells expressing eGFP and mCherry FP at similar concentrations. (*Gray hatching*) The different PIE channels. (B) Confocal macrotime images of HeLa cells expressing eGFP and mCherry with photons from the $F_{GG}(t)$ (eGFP) and $F_{RR}(t)$ (mCherry) PIE channels. (*Open box*) Subcellular region where PIE-FI was performed. Various correlation functions are shown for PIE-RICS experiments performed in live cells expressing (*C*) eGFP and mCherry at similar concentrations, (*D*) with an excess of eGFP, (*E*) eGFP-mCherry tandem construct, and (*F*) mVenus-mCherry tandem construct. Error bars represent the standard deviation and were used for weighted fitting to Eq. 2. In panels *D* and *F*, top views of selected CCFs are shown. The plus-sign in the figure legend indicates the combination of PIE channels into a single macrotime image, while the multiplier sign indicates the cross-correlation calculation of two macrotime images.

combined $F_{GR+RR}(t)$ PIE channel (see Table S1 for the expected β); and N_{R_T} is the total number of molecules carrying a red fluorophore. The higher the f_{G_T,R_T} or β, the more the red spatial ACF amplitude will deviate from the normal curve where the amplitude is inversely proportional to

N_{R_T}. The amplitude of G_{RR} in the absence of crosstalk (Fig. 2 C, *red curve*) is simply defined as

$$G_{RR}(0,0) = \frac{1}{N_{R_T}}. \tag{6}$$

The $G_{RR}(\xi,\psi)$ ACF scales inversely, and only with N_{R_T}, making it straightforward to calculate the absolute concentration when PIE-RICS is used. We performed a similar experiment in cells expressing eGFP in considerable excess with respect to mCherry (Fig. 2 D). In this case, a concentration calculated from the amplitude of G_{GR+RR} would be far from the absolute value without correcting for crosstalk. A concentration calculated from the amplitude of G_{RR}, however, is still independent of crosstalk.

The spatial cross-correlation function

When PIE is not used for the cross-correlation analysis, a false-positive cross-correlation amplitude is clearly observed as shown in Fig. 2, C and D (gray curves) when the $F_{GG}(t)$ and $F_{GR+RR}(t)$ PIE channels were used for determining the images. When the crosstalk-free $F_{GG}(t)$ and $F_{RR}(t)$ PIE channels are used instead, this amplitude drops below the background level (Fig. 2, C and D, black curves and Fig. 2 D, top views). Thus, even in cells with a large overexpression of eGFP, no false-positive cross-correlation is observed when PIE was used.

As a positive control, we analyzed the eGFP-mCherry fusion protein, which is known to constitute a good model FP pair for both dual-color fluorescence cross-correlation spectroscopy (30) and FRET (31) (Fig. 2 E). The high amplitude of the $G_{GG\times RR}(\xi,\psi)$ crosstalk-free spatial CCF confirms the linked diffusion of the two fluorescent proteins. This amplitude is given by (13)

$$G_{GG\times RR}(0,0) = \left(\frac{1-f_E}{1-f_E f_{GR,G_T}}\right)\frac{N_{GR}}{N_{G_T}N_{R_T}}, \qquad (7)$$

where f_E is the FRET efficiency; N_{G_T} is the total number of molecules carrying a green fluorophore; and f_{GR,G_T} is the fraction of double-labeled molecules N_{GR} versus N_{G_T}. FRET and/or incomplete double-labeling thus influence the observed cross-correlation amplitude. Assuming the FRET-lowered brightness of the eGFP in the $F_{GG}(t)$ PIE channel is compensated by the FRET-increased brightness of mCherry FP in the $F_{GR}(t)$ PIE channel, $G_{(GG+GR)\times RR}(0,0)$ can be defined as

$$G_{(GG+GR)\times RR}(0,0) = \frac{N_{GR}}{N_{G_T}N_{R_T}}. \qquad (8)$$

Hence, the absolute concentration of double-labeled species can be calculated from Eq. 8, even if f_E and f_{GR,G_T} are not known. It can be seen in Fig. 2 E that the amplitude $G_{(GG+GR)\times RR}$ (cyan curve) is indeed slightly higher than that of $G_{GG\times RR}$ (black curve). Thus, under the right conditions, Eq. 8 represents the CCF amplitude as if no FRET or cross-talk were occurring, and can be used for straightforward quantification of interactions.

The spatial ACF of the green fluorophore in the presence of FRET

The amplitude of the spatial ACF from the macrotime image with $F_{GG}(t)$ photons when the system undergoes FRET is given by

$$G_{GG}(0,0) = \left(\frac{1+\left(f_E^2-2f_E\right)f_{GR,G_T}}{\left(1-f_E f_{GR,G_T}\right)^2}\right)\frac{1}{N_{G_T}}. \qquad (9)$$

Again, assuming the FRET-lowered brightness of eGFP in the $F_{GG}(t)$ PIE channel is compensated by the FRET-increased brightness of mCherry FP in the $F_{GR}(t)$ channel, $G_{GG+GR}(0,0)$ is given by

$$G_{GG+GR}(0,0) = \frac{1}{N_{G_T}}. \qquad (10)$$

Under conditions of incomplete double-labeling and in the presence of FRET, concentrations calculated from $G_{GG}(0,0)$ will be too low whereas the correct and absolute concentrations can be calculated with $G_{GG+GR}(0,0)$, even if f_E and/or f_{GR,G_T} are not known. The effect of FRET on the green ACF can be seen in Fig. 2 E where the amplitudes of G_{GG} (green curve) and G_{GG+GR} (blue curve) are slightly offset.

eGFP-mCherry versus mVenus-mCherry

PIE-FI is not limited to dual-color imaging of fluorophores with significantly separated emission spectra such as eGFP and mCherry, but can also be performed on constructs with significantly more crosstalk provided the green emission filter still blocks all photons coming from the red fluorophore. To demonstrate this, we measured the cross-correlation PIE-RICS of a mVenus/mCherry tandem. The crosstalk of mVenus into the red detection channel is significantly higher than that of eGFP because its emission spectrum is more red-shifted (see Table S1). In cells expressing an mVenus-mCherry tandem, a high CCF amplitude was observed, even higher than for eGFP-mCherry (Fig. 2 F). This suggests a higher fraction of double-labeled species exist. Additionally, the difference when correcting the green ACF and CCF for FRET was bigger than for eGFP-mCherry, suggesting a higher f_E. We analyzed the ACFs and CCF quantitatively with Eqs. 6, 8, and 10 to assess the percentage of species having a fluorescent green and red fluorophore (Table 1). We calculated f_{GR,G_T}, the percentage of fluorescent eGFP molecules that are attached to a fluorescent mCherry, and f_{GR,R_T}, the percentage of fluorescent mCherry molecules that are attached to a fluorescent eGFP. For

TABLE 1   Dual-color PIE-RICS analysis

Protein	f_{GR,G_T} [%]	f_{GR,R_T} [%]
eGFP-mCherry	37 ± 4	73 ± 8
mVenus-mCherry	48 ± 7	85 ± 11

mVenus-mCherry, both f_{GR,G_T} and f_{GR,R_T} were higher than for eGFP-mCherry. It is known that mVenus folds and maturates more efficiently than eGFP, which would explain the larger fraction of fluorescent mVenus in the tandem constructs (17). The reason for the larger fraction of fluorescent mCherry in the mVenus-mCherry construct might be due to a more efficient folding of mCherry when attached to mVenus.

Dual-color PIE-RICS is definitely the more robust approach for quantifying such protein-protein interactions inside cells, because there can be a significant crosstalk if different fluorescent proteins are used as labels and because any effect of FRET can be removed from the experimental data. Also, because PIE-FI allows a straightforward, quantitative analysis of fluorophores, even with limited spectral separation, it holds great promise for multicolor imaging. Fluorescence cross-correlation analysis methods, when performed properly, allow the determination of binding affinities, even in live cells (30,32,33). In the past, quantification of intracellular binding affinities has proven difficult because of the presence of crosstalk and/or FRET (32,33), which can be simplified with PIE-FI. Fluctuation measurements on ternary complexes have mostly been limited to the theory and proof-of-principle experiments (34,35). The application of PIE-FI has the potential for imaging multiple fluorophores simultaneously and quantitatively in cells for the study of, for example, ternary and perhaps even quaternary complexes.

Absolute brightness and stoichiometry measurements with PIE-NB

N&B analysis with PIE-FI

The same data that is used for RICS analysis can, in principle, be further analyzed with the number and brightness analysis (N&B) to extract the concentration and absolute brightness, and thus stoichiometry, of molecules and complexes (16). In general, the average molecular number image $n(x,y)$ and absolute brightness image $\varepsilon(x,y)$ can be calculated from the first and second moments of the pixel intensities,

$$n(x,y) = \frac{\langle I(x,y)\rangle_F^2}{\mathrm{var}(I(x,y))_F - \langle I(x,y)\rangle_F}, \qquad (11)$$

$$\varepsilon(x,y) = \frac{\mathrm{var}(I(x,y))_F - \langle I(x,y)\rangle_F}{\langle I(x,y)\rangle_F}, \qquad (12)$$

where

$$\langle I(x,y)\rangle_F = F^{-1}\sum_{f=1}^{F} I(x,y,f)$$

is the mean fluorescence intensity image and

$$\mathrm{var}(I(x,y))_F = F^{-1}\sum_{f=1}^{F}\left(I(x,y,f) - \langle I(x,y)\rangle_F\right)^2$$

is the temporal variance image of pixel (x,y) over all frames F in the image series. The temporal variance of the signal from a pixel is very sensitive to the statistics of photon emission, and photon counting detectors such as APDs have a nonnegligible dead time (36), which is even worse for time-correlated single-photon counting (TCSPC) electronics. Detection dead time reduces the number of detected photons and hence the measured variance at high count rates. Therefore, we investigated whether it is possible to perform a quantitative N&B analysis with PIE-FI.

We measured an aqueous solution of ATTO488 for 100 frames and calculated the histogram of the mean pixel intensity $\langle I(x,y)\rangle_F$ (Fig. 3 A) and a photon counting histogram (11.11 μs bin time) of the individual pixels (Fig. 3 B). Even at the relatively low average count rate of ~75 kHz, there is a significant probability that individual pixels have a high (approximately MHz) count rate. After calculating the images from the raw photon files and preceding PIE-NB brightness analysis, we calculated the dead-time-corrected pixel intensity $I_C(x,y,f)$ using (37),

$$I_C(x,y,f) = \frac{I_M(x,y,f)\tau_p}{1 - I_M(x,y,f)\tau_{\mathrm{dead}}}, \qquad (13)$$

where $I_M(x,y,f)$ is the measured photon count in pixel (x,y,f); τ_p is the pixel dwell time; and τ_{dead} is the dead time. The relation between the registered and corrected count rate per pixel as a function of dead time is illustrated in Fig. 3 C for a pixel dwell time of 11.11 μs. The effect of a 100-ns dead time correction on the experimental histograms is depicted in black in Fig. 3, A and B. To calibrate the dead-time characteristics of our hardware, we measured the whole-image average brightness for a broad dilution series of ATTO488 with Eq. 12 after correcting the image series with Eq. 13 using different values for τ_{dead} (Fig. 3 D). Two nonlinear regimes can be distinguished, at very low count rates (<10 kHz) and at very high count rates. Whereas the low signal nonlinearity has different origins (see Accurate Measurements at Picomolar Concentrations), a dead-time correction should correct the high count rate nonlinearity as seen for τ_{dead} ~100 ns (Fig. 3 D). This dead time corresponds well with the reported value for the TCSPC card that was used for the experiments (SPC-140, 100 ns; Becker & Hickl, Berlin, Germany).

The average PIE-NB brightness of the dye in the linear range of the concentration range was 75 ± 2 kHz/mol, when the dye was excited at 20 μW of 475-nm light. The average brightness calculated from a PIE-RICS analysis on the same data with Eq. 4 was slightly higher (82 ± 2 kHz/mol), suggesting that a pixel dwell time of 11.11 μs
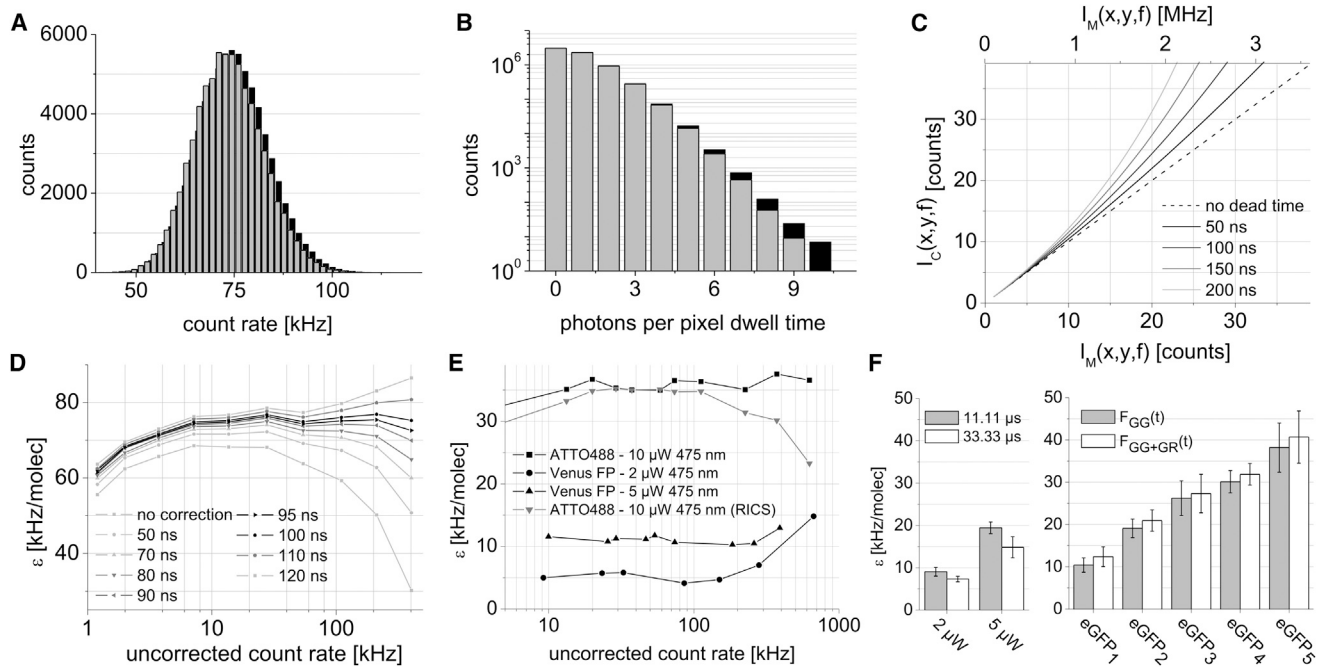
FIGURE 3   Determining the absolute molecular brightness with PIE-FI microscopy. (*A*) Histogram of the mean intensity per pixel from a series of 100 images of a 20-nM aqueous solution of ATTO488 at 20 μW excitation power and 11.11 μs pixel dwell time. (*B*) The photon counting histogram of absolute pixel counts for the same image series analyzed in panel *A*. (*Gray histograms*) Raw (not dead-time-corrected) data. (*Black histograms*) Same data corrected for a 100-ns detection dead time as given by Eq. 13. (*C*) The relationship between the measured (I_M) and corrected (I_C) photon counts is plotted assuming a pixel dwell time of 11.11 μs for different detection dead times. The *x* axis is displayed in counts per pixel dwell time (*lower axis*) and in megacounts per second (*upper axis*). (*D*) The experimental dependence of the measured brightness of ATTO488 determined from samples of various concentration (and hence count rate) assuming different detection dead-time corrections. (*E*) Dead-time-corrected brightness analysis of ATTO488 and Venus FP in a 10-cP buffer. (*F*) Molecular brightness measurements of eGFP and eGFP oligomers in live cells. (*Left bar chart*) Dependence of the apparent monomeric eGFP brightness on laser power and pixel dwell time. (*Right bar chart*) Molecular brightness for different eGFP tandem constructs ranging from monomers to pentamers.

is still too long to accurately sample the temporal pixel variance needed for proper PIE-NB brightness for a freely diffusing fluorophore in solution. When analyzing the same dye in 10-cP buffer, the PIE-NB brightness (36 $\pm$ 1 kHz/mol) and PIE-RICS brightness (35 $\pm$ 1 kHz/mol) at 10 μW excitation power were in the linear range and indeed very similar, demonstrating that it is possible to measure the brightness accurately with PIE-FI, either from the spatial (PIE-RICS) or the temporal (PIE-NB) pixel variance (Fig. 3 *E*). In the 10-cP buffer, we studied the brightness of Venus FP at two laser powers. The average brightness was 5.1 $\pm$ 0.8 kHz/mol at 2 μW and 11.0 $\pm$ 0.5 kHz/mol at 5 μW, agreeing well with what was obtained from the PIE-RICS experiments (Fig. 1 *F*).

PIE-NB in cells

Using proper correction for the large dead time of the TCSPC detection system used for PIE, we tested the performance of PIE-NB in living cells expressing eGFP. For the N&B analysis, images need not be spatially homogeneous as for RICS analysis, but it is still necessary to remove variance due to drift of the cell and the slow motion of large cellular structures (16). As very few photons are typically

detected per pixel with PIE-FI, it is helpful to use spatial averaging as well as temporal averaging to remove slow fluctuations (see Eq. S6 in the Supporting Material). Spatial averaging can be done as the pixel size is generally fivefold less than the radial waist of the PSF.

First, we measured the effect of laser power and pixel dwell time on the obtained apparent eGFP brightness. The measured brightness at a 11.11-μs pixel dwell time and 2 μW or 5 μW excitation power (Fig. 3 *F*, *left panel*) were similar to what was expected considering the performance of the microscope (see Table S1). A longer pixel dwell time reduced the apparent PIE-NB brightness due to motion of the eGFP in the PSF while measuring at the pixel.

Brightness analysis of eGFP oligomers in cells

We used PIE-NB to investigate the molecular brightness of different homo-oligomers of eGFP, which have been previously used for characterizing the cytosolic dynamics of large rod-like molecules (38) (Fig. 3 *F*, *right panel*). The PIE-NB brightness of the oligomers increased with size, although their brightness was not an integer multiple of the monomer brightness. It is known that not all fluorescent proteins mature and fluoresce. We used the measured

brightness to estimate the average maturation efficiency of eGFP using

$$\varepsilon(n) = \varepsilon(1) \frac{np}{1 - (1 - p)^n},$$ (14)

where $\varepsilon(n)$ is the observed brightness of the n-mer; $\varepsilon(1)$ is the brightness of a monomer; and p is the maturation probability. The maturation probabilities estimated from measurements on the dimer were ~91%, for the trimer 84%, and for the tetramer and pentamer ~73%. Interestingly, the brightness does not continue linearly with oligomer size. This suggests that higher-order oligomer constructs have a more difficult time maturating than monomers or dimers. Alternatively, it is also possible that the decrease in the molecular brightness for the higher order oligomers is due to an increasingly higher probability for singlet-singlet or singlet-triplet annihilation, as has been proven before for dendrimers (39) and DsRed tetramers (40). Taken together, these experiments demonstrate that quantitative N&B analysis can be performed with PIE-FI, when the appropriate dead-time correction is applied.

Using the fluorescence lifetime information from PIE-FI

Accurate measurements at picomolar concentrations

The fluorescence lifetime information available from PIE with TCSPC detection brings additional benefits when performing PIE-FI experiments. One example is measurements at picomolar concentrations. At low signal, uncorrelated noise (Raman scattering, laser reflections, detector dark

counts, background light) or correlated noise (detector after-pulsing) contaminates the fluorescence signal, as can be seen in a microtime histogram of a PIE-FI series of an aqueous solution of ATTO488 for concentrations varying from 100 nM to 6.1 pM (Fig. 4 A). Whereas at high concentration (100 nM) most detected photons are coming from fluorescence, at low (195-pM, 100-nM diluted 2^9-fold) and very low (6.1-pM, 100-nM diluted 2^{14}-fold) concentrations, the scattering signal makes up a larger fraction of the detected photons. Correcting for scattering is difficult due to the nonlinear weighting of the different species in a correlation analysis. The amplitude of the PIE-RICS ACF determined over four orders of magnitude in concentration is shown in Fig. 4 B. Due to scattering, the amplitude does not vary linearly with concentration below ~1 nM. One way to reduce the effect of noise is to use time gating. The scattering photons come immediately with the excitation pulse, whereas the majority of fluorescence photons are delayed. By selecting photons that arrive after the instrument response function (IRF) has decayed, as illustrated with the $F_{GG,gated}(t)$ channel in Fig. 4 A, it is possible to suppress the detection of scattered photons and perform quantitative measurements at subnanomolar concentrations (Fig. 4 B).

A very elegant approach to avoid problems with scattering during the correlation analysis is to use a lifetime weighting approach as was done previously in fluorescence lifetime correlation spectroscopy (FLCS) (41). This is possible, as long as a filter pattern can be designed that differs substantially between the different species (42,43). In raster lifetime image correlation spectroscopy (RLICS), each photon in the macrotime image is weighted by the
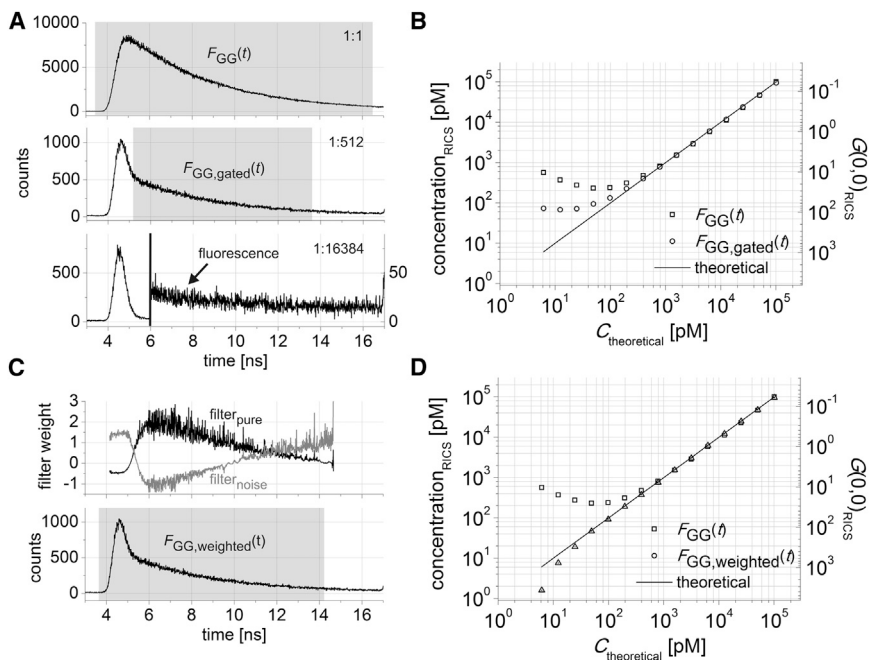

FIGURE 4 Measuring picomolar concentrations with RLICS. (A) Experimental microtime histograms of a 100-nM (top), 195-pM (middle), and 6-pM (bottom) ATTO488 solution. (Shaded hatching) Nongated and gated $F_{GG}(t)$ PIE channels. At 6 pM, the y scale was expanded 10 times from 6 ns onward to show the fluorescence. (B) Theoretical versus RICS-measured concentration of a dilution series of ATTO488 from 100 nM to 6 pM in twofold dilution steps with photons from the respective hatched PIE channels in panel A. For reference, the experimental $G_{GG}(0,0)$ value from the RICS experiment determined by fitting the ACF to Eq. 2 is given on the right y axis. (C) (top) Experimental lifetime weighting filters calculated from the data in the $F_{GG}(t)$ PIE channel (bottom). (D) Theoretical versus measured concentration for the same dilution series as in panel B, when lifetime weighting is used. The nonweighted data and experimental $G_{GG}(0,0)$ from the RICS experiment are given for comparison.

species filter (Fig. 4 *C* and see Eq. S8 in the Supporting Material), dependent on the microtime of the detected

PIE channel (for eGFP or mVenus) or the $F_{RR}(t)$ PIE channel (for mCherry),

$$F_{\text{fit}}(t) = N_p \left[(1 - f_s) \frac{irf(t - t_{\text{shift}}) * \sum_{x=1}^{n} (f_x \exp(-t/\tau_x)) + c}{\sum_{i=1}^{T} \left[irf(t_i - t_{\text{shift}}) * \sum_{x=1}^{n} (f_x \exp(-t_i/\tau_x)) + c \right]} + f_s \frac{irf(t - t_{\text{shift}})}{\sum_{i=1}^{T} (irf(t_i - t_{\text{shift}}))} \right], \quad (17)$$

photon. As the filters can have negative values, it is possible that the total pixel intensity after filtering is very close to zero, or even zero, which would adversely affect the amplitude of the ACF. Therefore, we first apply a precorrelation image rescaling

$$I(x, y, f)_{\text{scaled}} = I(x, y, f) + \min(I), \quad (15)$$

where $\min(I)$ is the absolute value of the lowest pixel intensity in the image series. Spatial ACFs were then calculated per frame with Eq. 1 and the average spatial ACF over all frames was rescaled to its original amplitude (44),

$$\langle G(\xi, \psi) \rangle_F = \frac{(\langle I \rangle_{XYF} + \min(I))^2}{(\langle I \rangle_{XYF})^2} \langle G(\xi, \psi) \rangle_{\text{scaled}}, \quad (16)$$

where

$$\langle I \rangle_{XYF} = (XYF)^{-1} \sum_{f=1}^{F} \sum_{y=1}^{Y} \sum_{x=1}^{X} I(x, y, f)$$

is the spatially averaged pixel intensity over all frames F. The PIE-channel selected for the analysis and the RLICS amplitude as a function of concentration are shown in Fig. 4, *C* and *D*. Clearly, the range at which the concentration could be accurately determined was significantly improved to <~30 pM. Considering an image size of 156.25 μm^2, this corresponds to an average of $N < 10$ molecules in the whole image. Below ~30 pM concentration, the measured concentrations were lower than expected, most likely due to dilution artifacts at low concentration.

Resolving FRET species with lifetime-weighted PIE-FI

The fluorescence lifetime information available with PIE makes it possible to quantify FRET in PIE-FI experiments. We demonstrate this by further analyzing the eGFP/mCherry and mVenus/mCherry data presented in Fig. 2. First, from cells coexpressing mCherry and either eGFP or mVenus, we extracted the fluorescence lifetime of the respective protein in the absence of FRET by performing a convolution fitting (i.e., Eq. 17 with $n = 1$) of the microtime histogram constructed with all photons from the $F_{GG}(t)$

where N_p is the total number of photons in the decay; f_s is the fraction of scattering in the decay; t_{shift} is the temporal shift of the IRF; the asterisk is the convolution function; c is the contribution of uncorrelated background; f_x and τ_x are the fractional contribution and excited state fluorescence lifetime of component i; n is the number of lifetime components; and T is the number of time channels included in the fitting (45). The values $f_s, f_x, \tau_x,$ and c were allowed to vary during fitting. The fluorescence decay of eGFP and mVenus could be approximated well with a single exponential (Fig. 5, *A* and *B*, and Table 2) and the resulting lifetimes agreed well with reported values (46,47). The fluorescence decay of mCherry in the $F_{RR}(t)$ PIE channel could be fitted reasonably well with a single exponential model and the recovered lifetime was 1.50 ± 0.06 ns, close to what has been reported as the major component governing the fluorescence decay of mCherry (25).

In cells expressing the heterodimer tandems, the fluorescence of the green fluorophore was quenched by the close proximity of the mCherry FRET acceptor (Fig. 5, *A* and *B*). A biexponential model was necessary to fit the fluorescence decay (Eq. 17 with $n = 2$), yielding one fluorescence lifetime close to that of the donor-only species and one strongly quenched fluorescence lifetime (Table 2). From the lifetimes values, the FRET efficiency was determined:

$$f_E = 1 - \frac{\tau_{DA}}{\tau_D}. \quad (18)$$

For eGFP-mCherry, $f_E = 0.55$ was close to the previously reported value of a similar construct (Table 2) (46). The mVenus/mCherry pair clearly exhibited a higher f_E of 0.63, consistent with the higher calculated R_0 for the mVenus/mCherry pair (see Table S1). The fraction of the donor fluorophore population exhibiting a fast lifetime component was similar for both samples, suggesting that mCherry acts equally well as a FRET acceptor in both constructs. To verify whether the photophysical properties of mCherry are independent of the presence of the proximal FRET donor, we also analyzed its fluorescence lifetime directly in the tandem constructs. For all constructs, the directly excited fluorescence lifetime of mCherry stayed constant (Table 2).
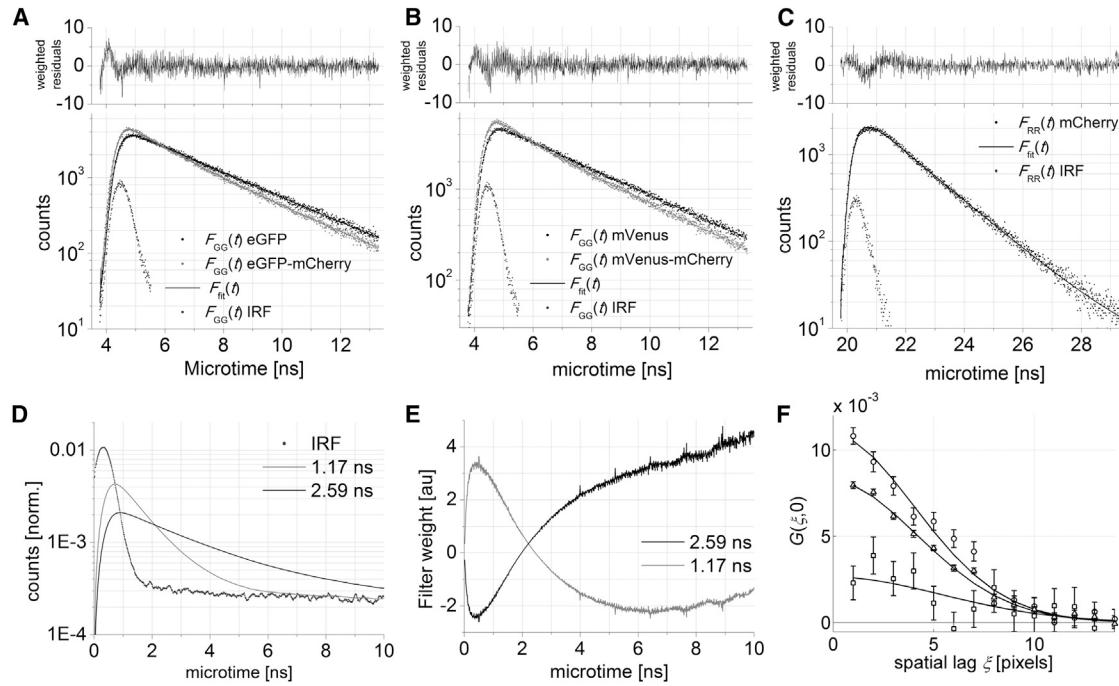
FIGURE 5 Dual-fluorophore pseudo-FLIM and dual-color RLICS analysis. Fluorescence lifetime analysis of image data for (*A*) eGFP and eGFP-mCherry, (*B*) mVenus and mVenus-mCherry, and (*C*) mCherry. (*D*) Calculated idealized fluorescence decay of FRET-quenched (1.17 ns) and unquenched (2.59 ns) eGFP in an eGFP-mCherry tandem convoluted with the experimental IRF. (*E*) Lifetime weighting filters calculated from the data in panel *D*. (*F*) Unfiltered (*triangles*), FRET-species filtered (*circles*), and non-FRET species filtered (*squares*) $G_{GG\times RR}(\xi,0)$ of the eGFP-mCherry tandem measured in live cells.

Species-RICS in cells

It is possible to separate different species with the same color during FCS experiments based on their fluorescence lifetime with FLCS (41) or based on other parameters, such as their anisotrophy, with filtered FCS (48). With the lifetime information available in PIE-FI, we tested whether we can separate species based on their fluorescence lifetime inside living cells using a species-RICS approach. To do this, we analyzed a dual-color PIE-RICS dataset of cells expressing the eGFP-mCherry tandem dimer. Cross-correlation of mCherry with only those eGFP species having a quenched fluorescence lifetime should result in a higher CCF amplitude than the non-species-specific CCF. Likewise, cross-correlation with those eGFP species having a donor-only lifetime should result in a zero CCF amplitude.

Using the ideal fluorescence decay of eGFP and FRET-quenched eGFP convoluted with the IRF (see Eq. S7 in the Supporting Material) as input (Fig. 5 *D*), we created the two lifetime filters for the RLICS analysis (Fig. 5 *E*). Using the microtime histograms and weighting filters, we calculated two weighted macrotime image series of the donor, $I_{GG,D}(x,y,f)$, weighted for the non-FRET species and $I_{GG,DA}(x,y,f)$, weighted for the FRET species. The RLICS CCF with the (nonweighted) macrotime image series of mCherry, $I_{RR}(x,y,f)$ is shown in Fig. 5 *F*. The CCF amplitude indeed increased when weighting the data with the filter for the FRETing donor. Similarly when weighting the data with the filter for the nonFRETing donor, the CCF amplitude decreased. As the cross-correlation amplitude did not decrease to zero, this suggests that the

TABLE 2 Dual-color lifetime analysis

Protein	PIE channel	τ_1 [ns]	f_1 [%]	τ_2 [ns]	f_E	χ^2_r
eGFP	$F_{GG}(t)$	2.60 ± 0.04	—	—	—	2.01
eGFP-mCherry	$F_{GG}(t)$	2.59 ± 0.04	64 ± 4	1.17 ± 0.11	0.55 ± 0.04	1.54
eGFP-mCherry	$F_{RR}(t)$	1.46 ± 0.04	—	—	—	2.56
mVenus	$F_{GG}(t)$	2.99 ± 0.02	—	—	—	2.18
mVenus-mCherry	$F_{GG}(t)$	2.88 ± 0.03	64 ± 1	1.05 ± 0.11	0.63 ± 0.04	1.76
mVenus-mCherry	$F_{RR}(t)$	1.50 ± 0.02	—	—	—	1.97
mCherry	$F_{RR}(t)$	1.50 ± 0.06	—	—	—	2.73

Reconvolution fitting with Eq. 17 was performed on datasets with ~1E6 photons. The value $\tau_{1,2}$ is the fluorescence lifetime; f_1 is the fraction of the first lifetime component; f_E is the FRET efficiency, calculated with Eq. 18; and χ^2_r is the reduced fit quality parameter calculated from the anisotropy-free part of the fluorescence decay (45).

factor 2 difference in the fluorescence lifetime is not ideal for lifetime-weighted fitting. This proof-of-principle experiment shows that the fluorescence lifetime information encoded in a species-RICS experiment can be used to specifically study subspecies with the same color, yet different lifetimes.

CONCLUSION

In this work, we introduced pulsed interleaved excitation fluctuation imaging (PIE-FI), to our knowledge a novel microscopy modality in which we have combined PIE with existing techniques for fluctuation analysis such as RICS, ccRICS, N&B, and FLCS. We showed that RICS can be well performed using pulsed lasers. For fluorophores that are sensitive to photo-induced blinking and -bleaching, RICS shows definite advantages over single-point FCS measurements and the determined diffusion coefficient and brightness was more robust as a function of laser power. Crosstalk-free ccRICS could be performed with PIE, making it possible to directly obtain quantitative results from the amplitude of the ACFs and CCF. If direct excitation of the red fluorophore with green excitation is negligible, one can also correct for FRET when performing PIE-FI. The one disadvantage of using PIE-FI when performing an N&B analysis is the significant dead time of the TCSPC detection cards. However, by correcting for the effects of the dead-time, quantitative N&B analysis can be performed. From the quantitative results obtained from PIE-FI measurements, interactions and the stoichiometry of complexes can be determined. From the N&B measurement on different GFP oligomers, we could show that the folding efficiency of GFP decreases with the size of these oligomers.

In addition to the advantages of removing crosstalk for cross-correlation measurements, the TCSPC information available from the PIE-FI data can be used to enhance the functionality of fluctuation imaging experiments. Raster lifetime ICS (RLICS) has a dual advantage: the amount of uncorrelated noise does not need to be known a priori, and even correlated noise such as detector afterpulsing can be removed from the correlation function because, on the microtime level, it is detected as a constant offset in each time-to-amplitude converter channel. With RLICS we were able to perform quantitative concentration measurements down to <30 pM. In measurements of FP tandems in live cells, we used the lifetime information available in the PIE-RICS experiment to quantify the FRET efficiency. It was even possible to use lifetime filtering to discriminate between FRETing and non-FRETing complexes and analyze the species separately.

Of course, there are more imaging applications that can be enhanced using PIE than we have presented here. Recently, a new superresolution method based on fluctuation imaging has been introduced, stochastical optical fluctuation imaging (SOFI) (49,50). SOFI increases the res-

olution of an image series obtained using wide field microscopy when the fluorophores are stochastically blinking by analyzing the temporal correlation functions generated from pixels in the image. By combining SOFI with PIE, it would be possible to perform crosstalk-free multicolor SOFI. However, due to the slow imaging rates obtainable with the raster scanning implementation of PIE, SOFI-PIE may not be of practical use in this form. To overcome this difficulty, groups are working on the development of area detectors with lifetime resolution such as the one described by Michalet et al. (51) that would make PIE-SOFI possible. With the availability of the fluorescence lifetime information in PIE-SOFI, a multispecies SOFI analysis based on different labels distinguished based on their lifetime as in FLCS would be possible.

Altogether, PIE-FI provides new functionalities and enhances the analysis capabilities of different fluctuation imaging techniques. It is also straightforward to implement and can, in principle, be incorporated into any raster-scanning microscope (even commercial systems) as long as the scanning and detection modules can be synchronized (29,52,53). Therefore, we expect PIE-FI to become the new standard in advanced fluorescence microscopy.

SUPPORTING MATERIAL

REFERENCES

1. Elson, E. L., and D. Magde. 1974. Fluorescence correlation spectroscopy. I. Conceptual basis and theory. *Biopolymers.* 13:1–27.

2. Magde, D., E. L. Elson, and W. W. Webb. 1974. Fluorescence correlation spectroscopy. II. An experimental realization. *Biopolymers.* 13:29–61.

3. Magde, D., W. W. Webb, and E. Elson. 1972. Thermodynamics Fluctuations in a Reacting System-Measurement by Fluorescence Correlation Spectroscopy. *Phys. Rev. Lett.* 29:705–708.

4. White, J. G., W. B. Amos, and M. Fordham. 1987. An evaluation of confocal versus conventional imaging of biological structures by fluorescence light microscopy. *J. Cell Biol.* 105:41–48.

5. Petersen, N. O., P. L. Höddelius, …, K. E. Magnusson. 1993. Quantitation of membrane receptor distributions by image correlation spectroscopy: concept and application. *Biophys. J.* 65:1135–1146.

6. Wiseman, P. W., C. M. Brown, …, A. F. Horwitz. 2004. Spatial mapping of integrin interactions and dynamics during cell migration by image correlation microscopy. *J. Cell Sci.* 117:5521–5534.

7. Wiseman, P. W., J. A. Squier, …, K. R. Wilson. 2000. Two-photon image correlation spectroscopy and image cross-correlation spectroscopy. *J. Microsc.* 200:14–25.

8. Digman, M. A., P. W. Wiseman, …, E. Gratton. 2009. Detecting protein complexes in living cells from laser scanning confocal image sequences by the cross correlation raster image spectroscopy method. *Biophys. J.* 96:707–716.

9. Digman, M. A., P. W. Wiseman, …, E. Gratton. 2009. Stoichiometry of molecular complexes at adhesions in living cells. *Proc. Natl. Acad. Sci. USA.* 106:2170–2175.

10. Toplak, T., E. Pandzic, …, P. W. Wiseman. 2012. STICCS reveals matrix-dependent adhesion slipping and gripping in migrating cells. *Biophys. J.* 103:1672–1682.

11. Semrau, S., L. Holtzer, …, T. Schmidt. 2011. Quantification of biological interactions with particle image cross-correlation spectroscopy (PICCS). *Biophys. J.* 100:1810–1818.

12. Kapanidis, A. N., N. K. Lee, …, S. Weiss. 2004. Fluorescence-aided molecule sorting: analysis of structure and interactions by alternating-laser excitation of single molecules. *Proc. Natl. Acad. Sci. USA.* 101:8936–8941.

13. Müller, B. K., E. Zaychikov, …, D. C. Lamb. 2005. Pulsed interleaved excitation. *Biophys. J.* 89:3508–3522.

14. Kudryavtsev, V., M. Sikor, …, D. C. Lamb. 2012. Combining MFD and PIE for accurate single-pair Förster resonance energy transfer measurements. *ChemPhysChem.* 13:1060–1078.

15. Digman, M. A., C. M. Brown, …, E. Gratton. 2005. Measuring fast dynamics in solutions and cells with a laser scanning microscope. *Biophys. J.* 89:1317–1327.

16. Digman, M. A., R. Dalal, …, E. Gratton. 2008. Mapping the number of molecules and brightness in the laser scanning microscope. *Biophys. J.* 94:2320–2332.

17. Nagai, T., K. Ibata, …, A. Miyawaki. 2002. A variant of yellow fluorescent protein with fast and efficient maturation for cell-biological applications. *Nat. Biotechnol.* 20:87–90.

18. Enderlein, J., I. Gregor, …, J. Fitter. 2004. Art and artifacts of fluorescence correlation spectroscopy. *Curr. Pharm. Biotechnol.* 5:155–161.

19. Lamb, D. C., A. Schenk, …, G. U. Nienhaus. 2000. Sensitivity enhancement in fluorescence correlation spectroscopy of multiple species using time-gated detection. *Biophys. J.* 79:1129–1138.

20. Ivanchenko, S., and D. C. Lamb. 2011. Fluorescence correlation spectroscopy: principles and developments. *In* Supramolecular Structure and Function. J. Brnjas-Kraljevic and G. Pifat-Mrzljak, editors. Springer-Verlag, Berlin, Germany. pp. 1–30.

21. Thompson, N. L. 1991. Fluorescence correlation spectroscopy. *In* Topics in Fluorescence Spectroscopy. J. R. Lakowicz, editor. Plenum Press, New York.

22. Gielen, E., N. Smisdom, …, M. Ameloot. 2009. Measuring diffusion of lipid-like probes in artificial and natural membranes by raster image correlation spectroscopy (RICS): use of a commercial laser-scanning microscope with analog detection. *Langmuir.* 25:5209–5218.

23. Schwille, P., S. Kummer, …, W. W. Webb. 2000. Fluorescence correlation spectroscopy reveals fast optical excitation-driven intramolecular dynamics of yellow fluorescent proteins. *Proc. Natl. Acad. Sci. USA.* 97:151–156.

24. Hendrix, J., and D. C. Lamb. 2013. Pulsed interleaved excitation: principles and applications. *Methods Enzymol.* 518:205–243.

25. Hendrix, J., C. Flors, …, Y. Engelborghs. 2008. Dark states in monomeric red fluorescent proteins studied by fluorescence correlation and single molecule spectroscopy. *Biophys. J.* 94:4103–4113.

26. Petrásek, Z., and P. Schwille. 2008. Precise measurement of diffusion coefficients using scanning fluorescence correlation spectroscopy. *Biophys. J.* 94:1437–1448.

27. Ries, J., and P. Schwille. 2006. Studying slow membrane dynamics with continuous wave scanning fluorescence correlation spectroscopy. *Biophys. J.* 91:1915–1924.

28. Dertinger, T., V. Pacheco, …, J. Enderlein. 2007. Two-focus fluorescence correlation spectroscopy: a new tool for accurate and absolute diffusion measurements. *ChemPhysChem.* 8:433–443.

29. Brown, C. M., R. B. Dalal, …, E. Gratton. 2008. Raster image correlation spectroscopy (RICS) for measuring fast protein dynamics and concentrations with a commercial laser scanning confocal microscope. *J. Microsc.* 229:78–91.

30. Foo, Y. H., N. Naredi-Rainer, …, T. Wohland. 2012. Factors affecting the quantification of biomolecular interactions by fluorescence cross-correlation spectroscopy. *Biophys. J.* 102:1174–1183.

31. Tramier, M., M. Zahid, …, M. Coppey-Moisan. 2006. Sensitivity of CFP/YFP and GFP/mCherry pairs to donor photobleaching on FRET determination by fluorescence lifetime imaging microscopy in living cells. *Microsc. Res. Tech.* 69:933–939.

32. Oyama, R., H. Takashima, …, H. Yanagawa. 2006. Protein-protein interaction analysis by C-terminally specific fluorescence labeling and fluorescence cross-correlation spectroscopy. *Nucleic Acids Res.* 34:e102.

33. Shi, X., Y. H. Foo, …, T. Wohland. 2009. Determination of dissociation constants in living zebrafish embryos with single wavelength fluorescence cross-correlation spectroscopy. *Biophys. J.* 97:678–686.

34. Heinze, K. G., M. Jahnz, and P. Schwille. 2004. Triple-color coincidence analysis: one step further in following higher order molecular complex formation. *Biophys. J.* 86:506–516.

35. Hwang, L. C., M. Gösch, …, T. Wohland. 2006. Simultaneous multicolor fluorescence cross-correlation spectroscopy to detect higher order molecular interactions using single wavelength laser excitation. *Biophys. J.* 91:715–727.

36. Hillesheim, L. N., and J. D. Müller. 2003. The photon counting histogram in fluorescence fluctuation spectroscopy with non-ideal photodetectors. *Biophys. J.* 85:1948–1958.

37. Becker, W. 2005. Advanced Time-Correlated Single Photon Counting Techniques. Springer Series in Chemical Physics, Vol. 81. Springer, Heidelberg, Germany.

38. Pack, C., K. Saito, …, M. Kinjo. 2006. Microenvironment and effect of energy depletion in the nucleus analyzed by mobility of multiple oligomeric EGFPs. *Biophys. J.* 91:3921–3936.

39. Hofkens, J., M. Maus, …, F. De Schryver. 2000. Probing photophysical processes in individual multichromophoric dendrimers by single-molecule spectroscopy. *J. Am. Chem. Soc.* 122:9278–9288.

40. Cotlet, M., J. Hofkens, …, F. C. De Schryver. 2001. Identification of different emitting species in the red fluorescent protein DsRed by means of ensemble and single-molecule spectroscopy. *Proc. Natl. Acad. Sci. USA.* 98:14398–14403.

41. Böhmer, M., M. Wahl, …, J. Enderlein. 2002. Time-resolved fluorescence correlation spectroscopy. *Chem. Phys. Lett.* 353:439–445.

42. Kapusta, P., M. Wahl, …, J. Enderlein. 2007. Fluorescence lifetime correlation spectroscopy. *J. Fluoresc.* 17:43–48.

43. Rüttinger, S., P. Kapusta, …, R. MacDonald. 2010. On the resolution capabilities and limits of fluorescence lifetime correlation spectroscopy (FLCS) measurements. *J. Fluoresc.* 20:105–114.

44. Schwille, P., J. Korlach, and W. W. Webb. 1999. Fluorescence correlation spectroscopy with single-molecule sensitivity on cell and model membranes. *Cytometry.* 36:176–182.

45. Maus, M., M. Cotlet, …, C. A. Seidel. 2001. An experimental comparison of the maximum likelihood estimation and nonlinear least-squares fluorescence lifetime analysis of single molecules. *Anal. Chem.* 73:2078–2086.

46. Padilla-Parra, S., N. Audugé, …, M. Tramier. 2009. Quantitative comparison of different fluorescent protein couples for fast FRET-FLIM acquisition. *Biophys. J.* 97:2368–2376.

47. Sarkar, P., S. V. Koushik, …, Z. Gryczynski. 2009. Photophysical properties of Cerulean and Venus fluorescent proteins. *J. Biomed. Opt.* 14:034047.

48. Felekyan, S., S. Kalinin, …, C. A. Seidel. 2012. Filtered FCS: species auto- and cross-correlation functions highlight binding and dynamics in biomolecules. *ChemPhysChem.* 13:1036–1053.

49. Dedecker, P., G. C. Mo, …, J. Zhang. 2012. Widely accessible method for superresolution fluorescence imaging of living systems. *Proc. Natl. Acad. Sci. USA.* 109:10909–10914.

50. Dertinger, T., R. Colyer, …, J. Enderlein. 2009. Fast, background-free, 3D super-resolution optical fluctuation imaging (SOFI). *Proc. Natl. Acad. Sci. USA.* 106:22287–22292.

51. Michalet, X., R. A. Colyer, …, S. Weiss. 2009. Single-quantum dot imaging with a photon counting camera. *Curr. Pharm. Biotechnol.* 10:543–558.

52. Hendrix, J., and D. C. Lamb. Implementation and application of pulsed interleaved excitation for dual-color FCS and RICS. *In* Fluorescence Spectroscopy and Microscopy: Methods and Protocols. Y. Engleborghs and A.J.W.G. Visser, editors. Springer-Humana Press, Heidelberg, Germany. In press.

53. Gielen, E., N. Smisdom, …, M. Ameloot. 2008. Diffusion of myelin oligodendrocyte glycoprotein in living OLN-93 cells investigated by raster-scanning image correlation spectroscopy (RICS). *J. Fluoresc.* 18:813–819.

Pulsed interleaved excitation fluctuation imaging Supporting Material

Jelle Hendrix,[†] Waldemar Schrimpf,[†] Matthias Höller,[†] and Don C. Lamb[†§]

[†]Physical Chemistry, Department of Chemistry, Munich Center for Integrated Protein Science (CiPSM) and Center for Nanoscience (CeNS), Ludwig-Maximilians-Universität München, Butenandtstr. 11, Gerhard-Ertl-Building, D-81377 Munich, Germany.

[§]Department of Physics, University of Illinois at Urbana-Champaign, 1110 W. Green St., Urbana, IL 61801.

Supporting Materials and Methods

Reagents

The aqueous buffer contained 50 mM Na_2HPO_4, pH 7.5 and 50 mM NaCl. For the 10-cP buffer, 46% (w/w) sucrose (BioXtra 99.5%, Sigma-Aldrich Chemie GmbH Munich, Germany) was added. This buffer had a calculated viscosity of 10.28 centiPoise (cP) at 20 °C. Buffers exhibited a negligible fluorescence background. The gene of Venus FP was subcloned between *Eco*RI and *Hind*III restriction sites in a pRSET-B plasmid, expressed in JM109(DE3) cells (Promega, Leiden, The Netherlands) and the protein was purified via affinity chromatography (Ni^{2+} NTA, Qiagen, Venlo, The Netherlands) and stored in 50 mM Tris pH 7.5, 150 mM NaCl. Microscopy was performed in 8-well coverslips (#1 Nunc Lab-Tek Chambered Coverglass, Thermo Scientific, Braunschweig, Germany). Dyes employed in this work were ATTO488-COOH ($D = 370$ µm²/s at 22 °C, ATTO-TEC GmbH, Siegen, Deutschland) and Rhodamine B ($D = 394$ µm²/s at 22 °C, Sigma-Aldrich). For Venus FP, the coverslips were first incubated for 30 minutes with 1 mg/mL BSA (Sigma-Aldrich) to prevent non-specific absorption of the protein, and subsequently washed twice with the measurement buffer.

Cell culture

HeLa cells (NIH Reagent program) were cultivated in low-glucose DMEM (Life Technologies, Darmstadt, Germany) supplemented with 10% heat-inactivated fetal bovine serum at 5 % CO_2 and 37 °C in a humidified atmosphere. For transfection, 2×10^4 cells per well were plated in the morning in 8-well coverslips. Transfections were performed in the evening with Extreme Gene 9 transfection reagent (Roche Applied Science, Mannheim, Germany) and plasmid DNA. The peGFP-C1 plasmid was obtained from Clontech (Saint-Germain-en-Laye, France) The pmVenus-C1 plasmid was constructed by replacing the eGFP gene with an mVenus gene in the original peGFP-C1 plasmid. The peGFP-mCherry and mVenus-mCherry plasmids were constructed by subcloning the mCherry gene between *Eco*RI/*Bam*HI sites of peGFP-C1. At 12-16h post-transfection, the cell medium was exchanged with phenol red-free OptiMEM (Life technologies) and measurements were performed at room temperature.

PIE-FI microscope

A schematic of the PIE-FI microscope setup is shown in Fig. S1. The PIE-FI microscope was built around an Eclipse TE200 (Nikon) base. As an objective lens, a NA1.2 water immersion objective was used (Nikon CFI Plan Apo VC 60XWI). For green excitation, a pulsed Erbium-doped fiber laser with a fixed repetition rate of 27.4 MHz (FFS.SYS-CONT-COMP-TSHG, Toptica Photonics, Gräfelfing, Germany) was tuned to 561 nm to excite Rhodamine B or mCherry and served as the master clock for the laser driver module (Sepia II [PDL 828, SCM 828, SLM 828], Picoquant GmbH, Berlin, Germany) and the controller for the scanner. For blue excitation, a 475-nm pulsed diode laser (LDH-P-C-470) was used to excite ATTO488, eGFP or Venus. The blue laser was delayed ~18 ns electronically with respect to the green laser and was run just above the lasing threshold to ensure a narrow instrument response function. A low pass filter (KG5, Schott, Mainz, Germany) was used to remove any residual IR light from the 561 nm excitation beam. Laser powers were individually attenuated with continuous neutral density filter wheels (Thorlabs, Dachau/Munich, Germany), the laser beams were superimposed with a dichroic mirror (Chroma 500DCXR, AHF Analysentechnik) and coupled into the same single mode fiber (coupler: HRJC-23AF-400/700-P-20AC, fiber: QPMJ-A3A,3AF-488-3.5/125-3-5-1, OZ Optics, Ottawa, Canada). An achromatic broadband collimator (60FC-4-RGB11-47, Schäfter+Kirchhoff) ensured concentric and Gaussian beam profiles at the exit of the fiber. The excitation light was reflected towards the microscope with a polychroic mirror (Semrock Di01-R405/488/561/635, AHF Analysentechnik, Tübingen, Germany). The laser powers described in this work were measured after the polychroic mirror and are ~2.5× higher than in the sample. Fast X/Y beam scanning was achieved by placing two closely-spaced galvanometer scanners in the beam path (scanner: 6210H, controller: MicroMax 673 Series, Cambridge Technology, Planegg, Germany). The midpoint between the scanning mirrors was expanded and projected onto the back focal plane of the objective through an achromatic Keplerian telescope (achromatic lens doublets AC254-050-A and AC254-200-A, Thorlabs), slightly overfilling the back aperture. Emission light was descanned, transmitted through the polychroic mirror and focused on an 80-µm pinhole by a 100-mm achromatic lens (AC254-100-A, Thorlabs). After the pinhole, the fluorescence was recollimated, spectrally split (565DCXR, AHF), spectrally filtered and focused on avalanche photodiodes (SPCM-AQR-12 and SPCM-AQR-14, Perkin-Elmer). Each APD was connected to a separate TCSPC card (SPC-140, Becker&Hickl), eliminating the need for a routing bit in

the photon files and reducing dead-time effects. Furthermore, TCSPC cards were hardware triggered over a data acquisition device (USB-6008, National Instruments) to ensure synchronization. A Chroma ET520/40 (AHF) emission filter was used in the green channel while a Chroma ET630/75 (AHF) emission filter was used in the orange/red channel (Fig. S2). To efficiently suppress the detection of scattered laser light, these emission filters were chosen that blocked both lasers at least OD6. For the lifetime filtered RICS experiments, a Semrock Brightline 525/45 (AHF) was used in the green channel. The microscope was aligned by optimizing the PSF radii with point FCS measurements and the homogeneity of the scanning field was checked by evaluating the PSF at different positions in the image (Fig. S3). The scanner was controlled by an arbitrary waveform generating PCI board (M2i.6034, Spectrum Systementwicklung Microelectronic GmbH, Grosshansdorf, Germany). The data acquisition software for the dual-color PIE-FI setup that controls the TCSPC and PCI cards, was written in the C# language in Microsoft Visual Studio 2010. The software generated an ASCII info file as well as photon files for each TCSPC card per image frame, avoiding the generation of large files.

Image processing for correct RICS and N&B analysis

Removal of frames containing undesired heterogeneities

During RICS measurements, impurities or heterogeneities such as protein aggregates or vesicles occasionally diffuse through the region of interest. As the RICS correlation functions are determined on individual frames, frames with undesired heterogeneities can simply be deleted from the movie before the analysis is performed. To check for frames containing fluorescent heterogeneities, thresholding was performed. First of all, a spatial average was calculated for all frames:

$$\langle I(x,y,f)\rangle_{\Delta(XY)} = \frac{1}{(2\Delta X + 1)(2\Delta Y + 1)} \sum_{x=-\Delta X}^{\Delta X} \sum_{y=-\Delta X}^{\Delta X} I(x,y,f) \qquad \text{Eq. S1}$$

where ΔX and ΔY define the size of the averaging area. When the averaged pixel count in a spatially averaged region $\langle I(x,y,f)\rangle_{\Delta(XY)}$ was above a chosen threshold value, the frame was removed from the image series. For example, an averaging area ΔX, $\Delta Y = 2$ and a threshold

of 5 could be used to efficiently remove impure frames from a Venus FP sample with a 50-kHz average image intensity.

Image pre-processing for RICS

With RICS, the spatial fluctuation of photon counts in images is quantitatively analyzed. For experiments in live cells, slow motions of the cell itself or organelles within the cell can mask the motion one wishes to detect. Even immobilized particles will contribute to the RICS correlation functions. For an ideal RICS analysis, the spatial fluctuations should be only due to diffusion of the molecules of interest. To correct for immobile heterogeneities, an *immobile mean correction* was applied to the images (1):

$$I_{\text{RICS}}(x, y, f) = I(x, y, f) - \langle I(x, y) \rangle_F + \langle I \rangle_{XYF}, \qquad \text{Eq. S2}$$

where $I(x, y, f)$ is the photon count of pixel (x, y) in frame f, $\langle I(x,y) \rangle_F = \frac{1}{F} \sum_{f=1}^{F} I(x, y, f)$ is the 'mean image' with the mean pixel intensities over all frames F and $\langle I \rangle_{XYF} = \frac{1}{XYF} \sum_{x=1}^{X} \sum_{y=1}^{Y} \sum_{f=1}^{F} I(x, y, f)$ is the average intensity over all frames F. When inhomogeneities move slowly through the region of interest over the time scale of the experiment, the fast fluctuations in the whole image series can still be evaluated by performing a *moving average correction* (2):

$$I_{\text{RICS}}(x, y, f) = I(x, y, f) - \langle I(x, y, f) \rangle_{\Delta F} + \langle I \rangle_{XYF}, \qquad \text{Eq. S3}$$

where $\langle I(x, y, f) \rangle_{\Delta F} = \frac{1}{2\Delta F + 1} \sum_{f=-\Delta F}^{\Delta F} I(x, y, f)$ is the moving average series from frames (f-ΔF) to frame (f+ΔF) and $\langle I \rangle_{XYF}$ is the average pixel intensity of a region of $X \times Y$ over all frames F. This procedure removes slowly moving spatial inhomogeneities that might lead to an erroneous RICS calculation result. After this correction, the mean intensity of each image will be equal to the mean pixel intensity throughout the experiment.

Image pre-processing for N&B

For N&B analysis, the temporal pixel variance in a PIE-FI image should be determined by only the molecular diffusion and the shot noise of the experiment, which is distributed Poissonian (3). Assuming the intensity is homogeneously distributed in the image, slow

temporal variations in intensity due to sample photobleaching, drift or laser instability can be corrected using a *frame mean subtraction* followed by *addition of the mean pixel intensity over the entire experiment:*

$$I_{NB}(x,y,f) = I(x,y,f) - \langle I(f)\rangle_{XY} + \langle I\rangle_{XYF},$$ Eq. S4

where $I(x,y,f)$ is the photon count of pixel (x,y) in frame f, $\langle I(f)\rangle_{XY} = \frac{1}{XY}\sum_{x=1}^{X}\sum_{y=1}^{Y}I(x,y,f)$ is the average intensity of frame f and $\langle I\rangle_{XYF} = \frac{1}{XYF}\sum_{x=1}^{X}\sum_{y=1}^{Y}\sum_{f=1}^{F}I(x,y,f)$ is the average intensity over all frames F. When $\langle I\rangle_{XYF}$ is added to all pixels, the mean frame intensity will be constant while both the spatial and temporal pixel variance remains similar to the original data. When the image intensity is not distributed homogeneously, a local correction can be performed using a *per-pixel moving average subtraction followed by the addition of the pixel mean* (4):

$$I_{NB}(x,y,f) = I(x,y,f) - \langle I(x,y,f)\rangle_{\Delta F} + \langle I(x,y)\rangle_{F},$$ Eq. S5

where $\langle I(x,y,f)\rangle_{\Delta F} = \frac{1}{2\Delta F+1}\sum_{f=-\Delta F}^{\Delta F}I(x,y,f)$ is the moving average and $\langle I(x,y)\rangle_F = \frac{1}{F}\sum_{f=1}^{F}I(x,y,f)$ is the average intensity of pixel (x,y) over the whole image series. This correction preserves the spatial variance, and the variance from fast temporal fluctuations due to diffusing molecules. As the number of photons detected per pixel in a PIE-FI image is very low, even a moving average about a single pixel has insufficient statistics to reliably correct the N&B data. To circumvent this difficulty, one can perform spatial averaging in addition to the temporal moving average when the PSF is oversampled, as is the case for our N&B experiments:

$$I_{NB}(x,y,f) = I(x,y,f) - \langle I(x,y,f)\rangle_{\Delta(XYF)} + \langle I(x,y)\rangle_{F},$$ Eq. S6

where $\langle I(x,y,f)\rangle_{\Delta(XYF)} = (2\Delta X+1)^{-1}(2\Delta Y+1)^{-1}(2\Delta F+1)^{-1}\sum_{f=-\Delta F}^{\Delta F}\sum_{y=-\Delta Y}^{\Delta Y}\sum_{x=-\Delta X}^{\Delta X}I(x,y,f)$ is the mean pixel intensity in the cuboid with sides $2\Delta X+1$, $2\Delta Y+1$ and $2\Delta F+1$ surrounding pixel (x,y,f). For the experiments presented here, values of ΔX, $\Delta Y = 3$ and $\Delta F = 10$ were sufficient for a quantitative N&B analysis. After pre-processing the N&B data, the $n(x,y)$

and $\varepsilon(x, y)$ images can be further filtered using spatial averaging to increase the statistics per pixel and/or a median filter to remove outliers from the images.

Absolute concentration determination

With RICS and N&B, absolute concentrations can be determined. *In vitro*, the sample concentration is usually homogenously distributed and an uncorrelated fluorescent background can be assumed, the amplitude of the spatial ACFs/CCFs can be converted into concentrations without compromise. In cells, two conditions have to be fulfilled to quantitatively determine sample concentrations: (i) the absence of an immobile fraction has to be confirmed and (ii) any pre-analysis processing that is needed should not alter the temporal pixel variance encoded in the image by the diffusing molecules of interest. When, for example, a moving average correction is applied to RICS (Eq S 3), both these conditions are fulfilled when the spatial correlation image of this moving average does not exhibit significant correlation. Conversely, when the overall temporal variance of pixels is not significantly changed by any pre-analysis processing algorithm, one can assume that the concentration determined by the RICS analysis is correct.

Determination of weighted lifetime filters

A lifetime-weighted analysis requires determination of the appropriate weighting filters for the different species. To calculate the filters, the microtime spectra of the pure species needs to be determined or estimated. One possibility is to measure the pure species independently. For example, when performing measurements at low concentration, the microtime histogram from a highly concentrated sample could be used as species 1 ($F_{GG,1}(t)$) and the corresponding microtime histogram from a measurement of pure water can be used for species 2 ($F_{GG,2}(t)$). Alternatively, when the pure species cannot be determined independently, an idealized microtime histogram can be generated. For example, if the decay is expected to be monoexponential with known decay time, the microtime spectra of this species x can be determined by convoluting the theoretical decay with the instrument response function:

$$F_{GG,x}(t) = F_{GG,IRF}(t - t_{shift}) * \exp(-t / \tau_x)$$.   Eq. S7

Once the pure microtime histograms are known, the filters are determined using:

$$\begin{matrix} filter1 \\ filter2 \end{matrix} = \left(\begin{Vmatrix} F_{GG,1}(t) \\ F_{GG,2}(t) \end{Vmatrix} \cdot [D] \cdot \begin{Vmatrix} F_{GG,1}(t) \\ F_{GG,2}(t) \end{Vmatrix}^{T} \right)^{-1} \cdot \begin{Vmatrix} F_{GG,1}(t) \\ F_{GG,2}(t) \end{Vmatrix} \cdot [D] \qquad \text{Eq. S8}$$

where [D] is the diagonal matrix constructed from the reciprocal values of the corresponding histogram $F_{GG}(t)$ of a low-signal sample. The lifetime weighting filters used for quantitative RICS measurements at low concentration are shown in Fig. 4 *C* and estimations of the filters for the FRETing and non-FRETing eGFP-mCherry tandems are plotted in Fig. 5 *E*.

Supporting Table

Table S1 – Expected performance of the FPs on our PIE-FI microscope.

	$\varepsilon_{\lambda max}$ [M^{-1} cm^{-1}]	ϕ_F [%]	ε_{475nm} [%]	ε_{561nm} [%]	T [%]	$\varepsilon_{R/G}$ [%]	β [%]	R_0 [Å]
eGFP	55000	60	85	~0	61	2	5	51
mVenus	92200	57	24	~0	57	7	8	56
mCherry	72000	22	4	63	42	n.d.	100	

$\varepsilon_{\lambda max}$ is the extinction coefficient at the excitation maximum, ϕ_F is the fluorescence quantum yield, ε_{475nm} and ε_{561nm} are the percentage of maximum absorption at the laser wavelength, T is the calculated percentage of transmission for the FP through the polychroic, dichroic and its normal emission filter, $\varepsilon_{R/G}$ is the calculated relative brightness of the FP in the red versus the green detection channel, β is the calculated relative brightness of the FP versus mCherry FP in the red detection channel, *i.e.* the crosstalk (5), and R_0 is the calculated Förster radius when the FP is used with mCherry as a FRET acceptor. n.d. = not determined.
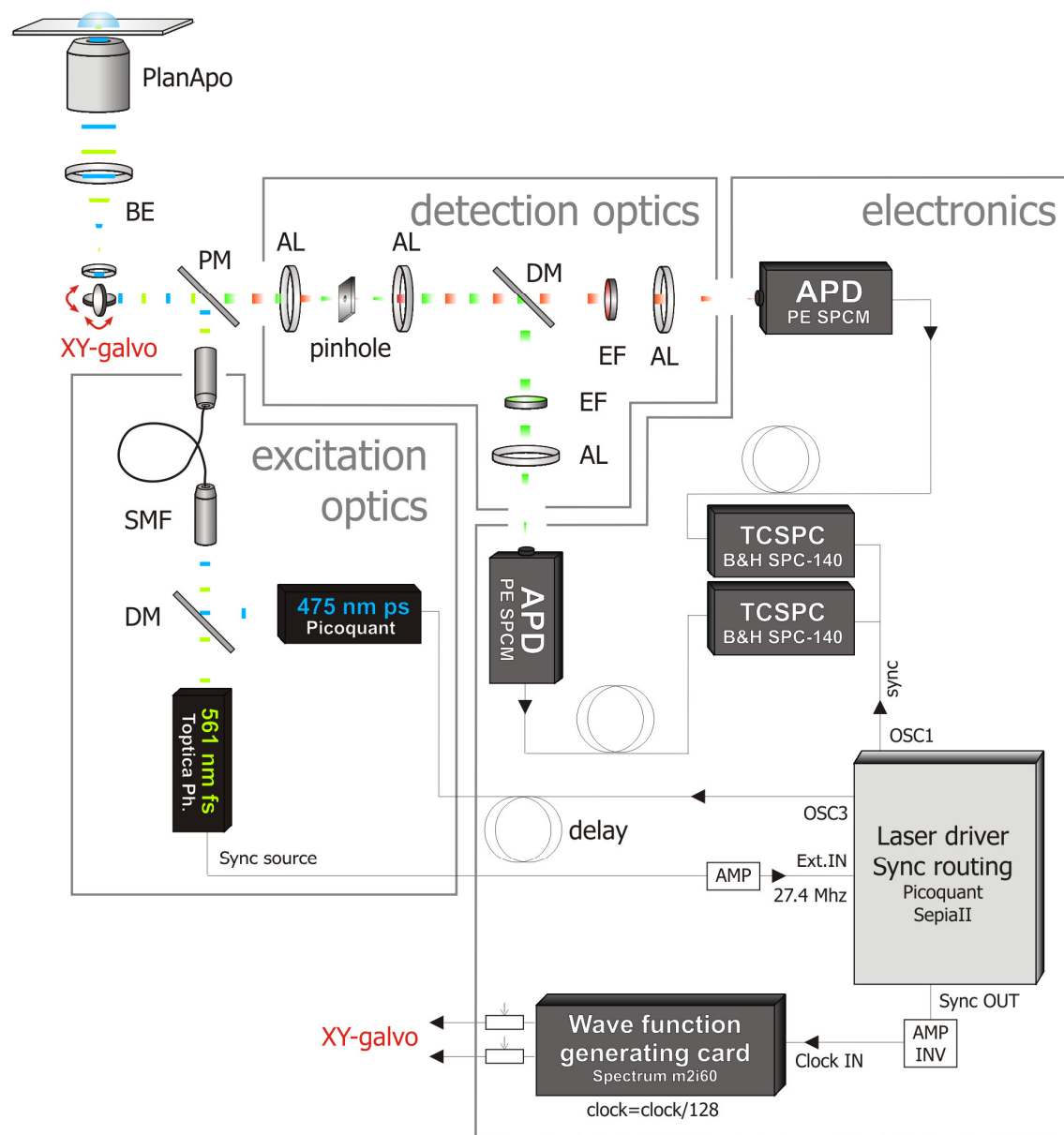
Supporting Figures

Fig. S1 – Schematic illustration of the PIE-FI setup used in this work. BE = beam expander, PM = polychroic mirror, AL = achromatic doublet lens, EF = emission filter, DM = dichroic mirror, SMF = single-mode fiber, OSC = oscillator module, AMP = signal amplifier, INV = signal inverter, galvo = galvanometric mirror scanner, APD = avalanche photodiode, sync = sychronization pulse.
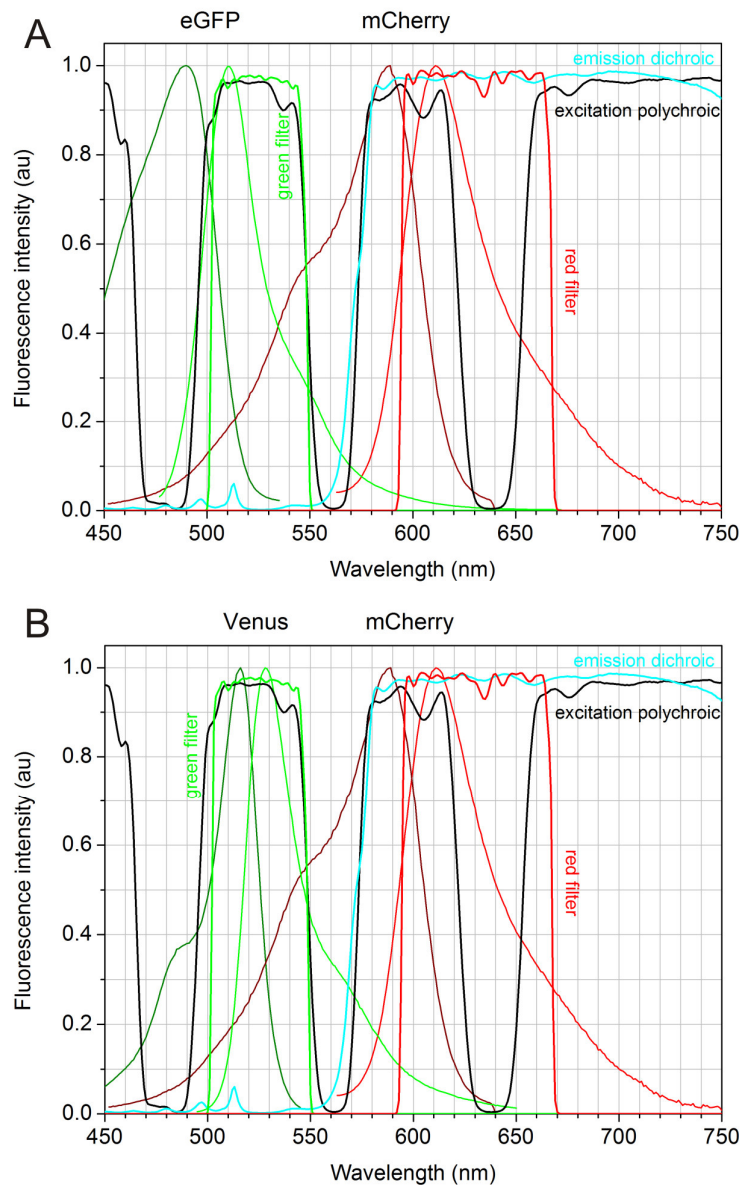
Fig. S2 – Excitation and fluorescence spectra of the FPs used in this work. The transmission spectra of the excitation polychroic, emission dichroic and emission filters, as described in the Supporting Materials and Methods section, were overlaid.
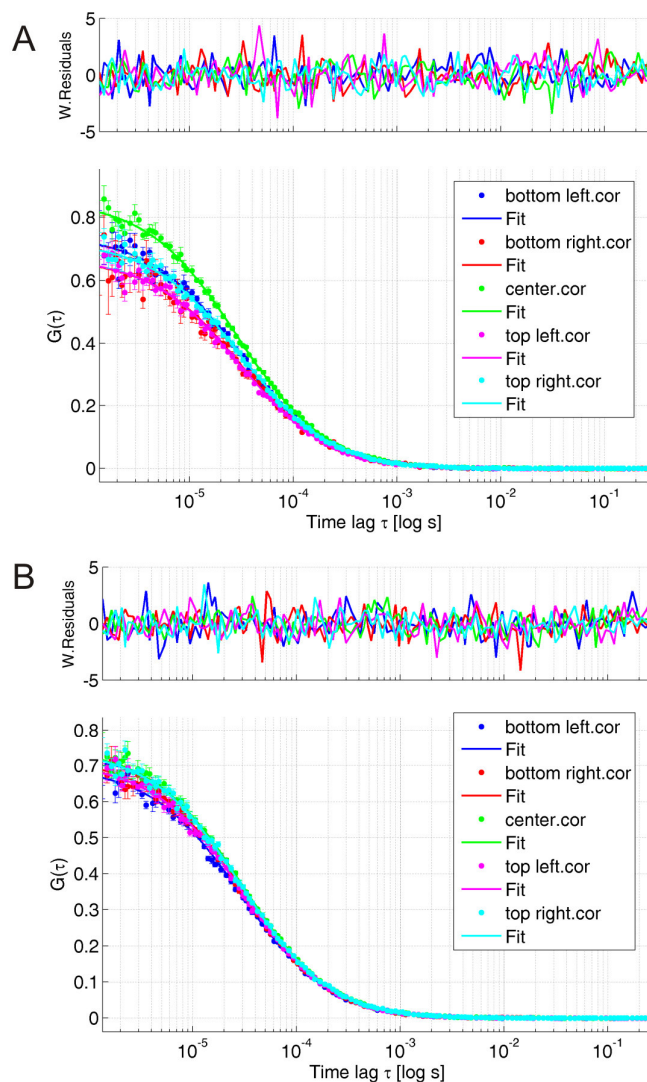
Fig. S3 – Verification of the galvo and telescope alignment with point-FCS. FCS ACFs of ATTO488 measured at the central or (0,0) position of the galvo scanner (drawn in *green*) or at the four respective corners (drawn in *blue, red, pink* and *cyan*) of a 100×100-µm² image (A) or 30×30-µm² image (B). The limited deviation in the corners confirmed a good alignment of the galvo and telescope in the excitation path. Importantly, all PIE-FI experiments were performed using a 12.5×12.5-µm² image range within the 100×100-µm² full range of the imaging system.
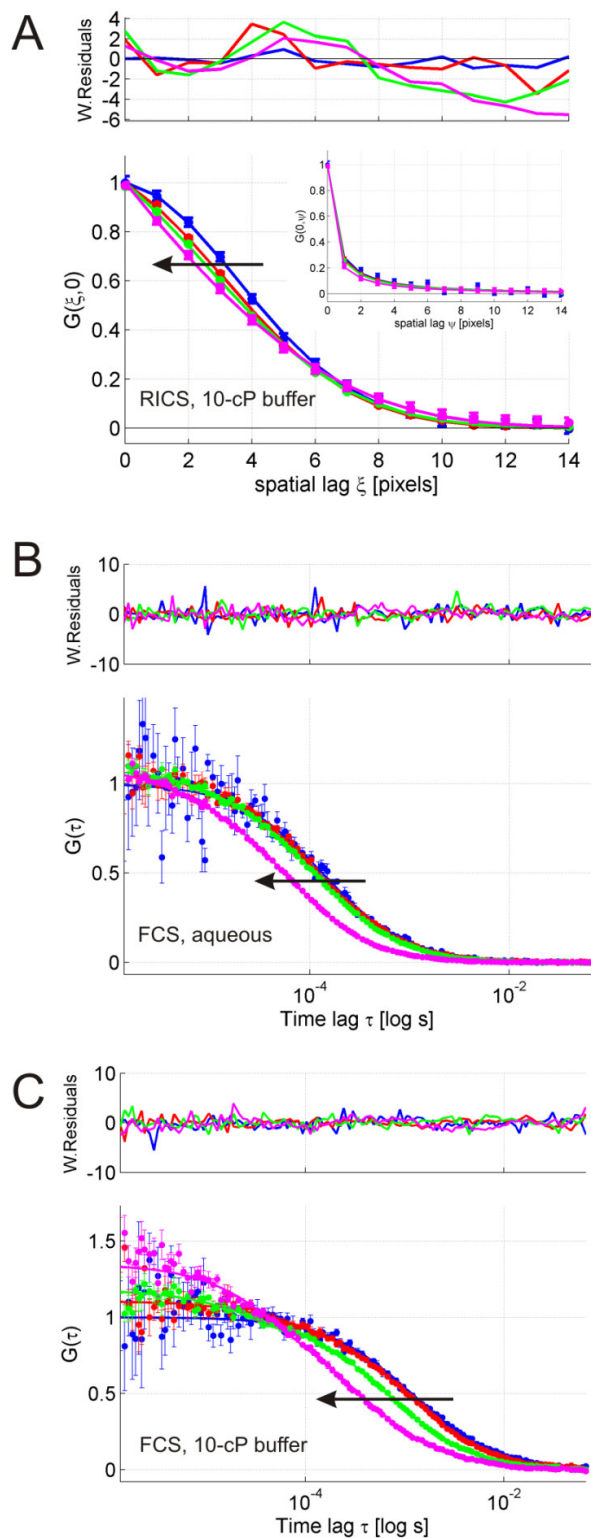
Fig. S4 – Performance of RICS and FCS for measuring Venus as a function of laser power in an aqueous or 10-cP buffer. (*A*) The experimental $G(\xi, 0)$ from PIE-RICS

(*symbols*) with fit (*line*) and weighted residuals is shown (*top graph*) for measurements at 2.5 µW (*blue*), 10 µW (*red*), 25 µW (*green*) and 100 µW (*pink*) excitation power. The $G(0, \psi)$ and fit are shown in the inset. The black arrow indicates the trend with increasing laser power. The correlation functions were normalized to the amplitude of the fit function by multiplying the data and fit with N(1-F$_{blink}$)/γ. (*B* and *C*) The experimental $G(\tau)$ from PIE-FCS (*symbols*) with fit (*line*) and weighted residual are shown (*top graph*) for measurements at 2.5 µW (*blue*), 10 µW (*red*), 25 µW (*green*) and 100 µW (*pink*) excitation power in aqueous solution (A) and in a 10-cp sucrose/buffer mixture (B). The black arrow indicates the trend with increasing laser power. The correlation functions were normalized to the amplitude of the fit function by multiplying the data and fit with N(1-F$_{blink}$)/γ.

Supporting References

1.   Digman, M. A., C. M. Brown, P. Sengupta, P. W. Wiseman, A. R. Horwitz, and E. Gratton. 2005. Measuring Fast Dynamics in Solutions and Cells with a Laser Scanning Microscope. Biophys J 89:1317-1327.
2.   Brown, C. M., R. B. Dalal, B. Hebert, M. A. Digman, A. R. Horwitz, and E. Gratton. 2008. Raster image correlation spectroscopy (RICS) for measuring fast protein dynamics and concentrations with a commercial laser scanning confocal microscope. J.Microsc. 229:78-91.
3.   Hillesheim, L. N. and J. D. Muller. 2005. The dual-color photon counting histogram with non-ideal photodetectors. Biophys J 89:3491-3507.
4.   Digman, M. A., R. Dalal, A. F. Horwitz, and E. Gratton. 2008. Mapping the Number of Molecules and Brightness in the Laser Scanning Microscope. Biophys J 94:2320-2332.
5.   Müller, B. K., E. Zaychikov, C. Bräuchle, and D. C. Lamb. 2005. Pulsed Interleaved Excitation. Biophys J 89:3508-3522.